The ASC inflammasome adapter controls the extent of peripheral protein aggregate deposition in inflammation-associated amyloidosis

Marco Losa[1], Marc Emmenegger[1], Pierre De Rossi[2,#], Patrick M Schürch[3,#], Tetiana Serdiuk[4,#], Niccolò Pengo[5], Danaëlle Capron[5], Dimitri Bieli[5], Niels J Rupp[6,7], Manfredi C Carta[1], Karl J Frontzek[1], Veronika Lysenko[3], Regina R Reimann[1], Asvin KK Lakkaraju[1], Mario Nuvolone[1,8], Gunilla T Westermark[9], K. Peter R. Nilsson[10], Magdalini Polymenidou[2], Alexandre P. A. Theocharides[3], Simone Hornemann[1], Paola Picotti[4], and Adriano Aguzzi[1,†]

[1] Institute of Neuropathology, University of Zurich, Zurich, Switzerland

[2] Department of Quantitative Biomedicine, University of Zürich, Zurich, Switzerland

[3] Department of Medical Oncology and Hematology, University Hospital Zurich, Zurich, Switzerland

[4] Institute of Molecular Systems Biology, Department of Biology, ETH Zurich, Zurich, Switzerland

[5] Mabylon AG, Schlieren, Zurich, Switzerland

[6] Department of Pathology and Molecular Pathology, University Hospital Zurich, Zurich, Switzerland

[7] Faculty of Medicine, University of Zurich, Zurich, Switzerland

[8] Amyloidosis Research and Treatment Center, Fondazione Instituto di Ricovero e Cura a Carattere Scientifico (IRCCS) Policlinico San Matteo, University of Pavia, Pavia, Italy

[9] Department of Medical Cell Biology, Uppsala University, Uppsala, Sweden

[10] Department of Physics, Chemistry and Biology, Linköping University, Linköping, Sweden

[#] Equal contribution

[†]Corresponding author: Adriano Aguzzi, Institute of Neuropathology, University of Zurich Schmelzbergstrasse 12, CH-8091 Zurich, Switzerland, E-mail: adriano.aguzzi@usz.ch

Abstract

ASC-containing inflammasomes form specks, extracellular aggregates which enhance the aggregation of Aβ amyloid in Alzheimer's disease. This raises the question whether ASC participates to additional aggregation proteinopathies. Here we show that ASC controls the extent of inflammation-associated AA amyloidosis, a systemic disease caused by the aggregation of the acute-phase reactant serum amyloid A (SAA). Using superresolution microscopy, we found that ASC colocalized tightly with SAA in human AA amyloidosis. Purified recombinant ASC specks accelerated SAA fibril formation *in vitro*. Mass spectrometry after limited proteolysis showed that ASC interacts with SAA via its pyrin domain. In a murine model of inflammation-associated AA amyloidosis, splenic AA amyloid load was conspicuously decreased in *Pycard*$^{tm1Vmd/tm1Vmd}$ mice which lack ASC. This reduction was not a consequence of enhanced amyloid phagocytosis, as SAA stimulation increased phagocytic activity in *Pycard*$^{+/+}$, but not in *Pycard*$^{-/-}$ macrophages. Treatment with anti-ASC antibodies decreased the amyloid loads in wild-type mice suffering from AA amyloidosis. The prevalence of natural anti-ASC IgG ($-\log EC_{50} \geq 2$) in 19,334 hospital patients was <0.01%, suggesting that anti-ASC antibody treatment modalities would not be confounded by natural autoimmunity. Higher anti-ASC titers did not correlate with any specific disease, suggesting that anti-ASC immunotherapy may be well-tolerated. These findings expand the role played by ASC to extraneural proteinopathies of humans and experimental animals and suggest that anti-ASC immunotherapy may contribute to resolving such diseases.

Introduction

Inflammation-associated amyloid A (AA) amyloidosis occurs in a heterogeneous spectrum of chronic conditions including inflammatory bowel disease, tuberculosis, hepatitis, genetic inflammatory diseases (e.g., familial Mediterranean fever), cancer as well as autoimmune diseases such as rheumatoid arthritis and vasculitis [1-3]. In these conditions, cytokines stimulate hepatocytes to synthesize and secrete Serum Amyloid A (SAA) into the bloodstream. During the acute-phase response, serum SAA can increase 1000-fold from its baseline concentration [4, 5]. Persistently high levels of SAA in serum can hamper its proper processing and clearance, leading to nucleation of aggregated AA fibrils and systemic deposition of AA amyloid. The deposition of amyloid in spleen, kidney, liver, and heart can be massive and cause life-threatening disruption of tissue integrity [6-8].

There is increasing evidence for an important role of innate immunity in the pathogenesis of protein misfolding diseases (PMDs) [9-13]. The adapter protein ASC (Apoptosis-associated speck-like protein containing a caspase recruitment domain) plays an eminent role in the pathogenesis of Alzheimer's disease (AD) [14-16]. Intrahippocampal injection of microglia-derived ASC specks leads to amyloid β (Aβ) cross-seeding in mice overexpressing Amyloid-β Precursor Protein and Presenilin-1 (APP/PS1;*Pycard*$^{+/+}$ mice) which is reduced in APP/PS1;*Pycard*$^{-/-}$ mice. This increase in Aβ pathology can be prevented by co-injection of ASC specks with anti-ASC antibodies [15, 17].

Aβ and AA amyloid consist of β-pleated sheets and have similar fibril sizes, fibril strand orientations, and cross-seeding capability [18]. Indirect evidence suggests a role for ASC in the pathogenesis of inflammation-associated (AA) amyloidosis. ASC was shown to colocalize with AA amyloid in kidney biopsies from patients with AA amyloidosis secondary to familial Mediterranean fever, where a gain-of-function mutation in the *Pyrin* gene activates ASC inflammasomes and leads to chronic overexpression of SAA [19]. Also, cryopyrin-associated periodic syndrome (CAPS) patients, owing to a genetic condition, have constitutively high NLRP3 and ASC inflammasome activation [20, 21] and are at high risk of developing AA amyloidosis [2]. SAA activates the NLRP3 inflammasome of human myeloid cells via an interaction with the P2X7 receptor, which induces ASC release *in vitro* through a cathepsin

B-sensitive pathway [22]. Additionally, the SAA cascade may prompt the upregulation of pro-inflammatory cytokines and enhances fibrillogenic activity towards SAA1 *in vitro* in murine macrophages [23, 24].

In a murine model of AA amyloidosis, subcutaneous administration of silver nitrate ($AgNO_3$), coupled with an intravenous application of preformed SAA fibrils (known as Amyloid Enhancing Factor or AEF), rapidly induces AA amyloidosis in spleen [25-27]. $AgNO_3$ serves as a proinflammatory stimulus that leads to elevation in SAA serum levels, while preformed AA fibrils (AEF) serve as a template for SAA aggregation [28]. Interestingly, depletion of splenic macrophages delays or inhibits AA amyloid accumulation in mice [25, 29] and macrophages can clear AA amyloid via Fc-receptor-mediated phagocytosis [30]. These results suggest that components of the innate immune system may control, both positively and negatively, the course of AA amyloidosis.

Here, we investigated the role of ASC in inflammation-associated amyloidosis *in vitro* and *in vivo.* We found that ASC forms complexes with SAA in post-mortem tissue of a patient with inflammation-associated AA amyloidosis, colocalizes with murine splenic AA amyloid, accelerates SAA fibril formation and interacts with SAA via its pyrin domain. *Pycard*$^{+/+}$ mice exhibited progressive splenic amyloidosis and a concomitant decrease in SAA serum concentration, both of which were attenuated in the absence of ASC. Treatment with anti-ASC antibodies decreased amyloid loads and improved health in a mouse model of amyloidosis, suggesting that anti-ASC immunotherapy may be useful in this condition.

Results

Colocalization of ASC with amyloid A

As ASC colocalizes with Aβ amyloid in mice and humans [15], we asked whether ASC would colocalize also with AA, a type of extraneural amyloid composed of SAA fibrils. We used the amyloidotropic dye Congo Red (CR) and antibodies against ASC to stain cardiac tissues from a patient suffering from vasculitis and systemic inflammation-associated AA amyloidosis and, for control, a 68-year-old male patient without any clinical sign of amyloidosis who died from left ventricular failure after myocardial infarction (**Fig. 1A**). CR-stained amyloidotic tissue, but not control tissue, showed a characteristic red appearance (**Fig. 1B**). ASC immunoreactivity was predominantly intramuscular and vascular, and appeared more pronounced in the amyloidosis patient. We then probed the potential colocalization between ASC and SAA using antibodies against ASC, SAA, and PAI-1 (as a vessel marker), as well as the amyloidotropic dye Thioflavin S. Two antibodies against ASC (polyclonal AL-177 and monoclonal MAB/MY6745 anti-ASC) and two antibodies against SAA (MAS41676 and DM003) were employed. We focused on areas in the proximity of vessels of an AA amyloidosis patient (**Fig. 1C**-**E**) and a control patient (**Fig. 1F** and **1G**). The integrated density, defined as the sum of the pixel values in immunofluorescence images, of ASC was slightly increased for the patient with amyloidosis. Both antibodies targeting SAA displayed a signal increase (**Fig. 1H**). The thioflavin S signal colocalized with SAA in the patient with AA amyloidosis, and to a lesser degree with ASC (**Fig. S1A**).

We then examined regions of high SAA intensity, presumptively corresponding to amyloid aggregates, by stimulated emission depletion (STED) microscopy (**Fig. 1I**-**L**). The resulting 3D model (**Fig. 1J** and **1L**) visualized the proximity of SAA and ASC within these aggregates. ASC was localized primarily in the periphery of amyloid aggregates, whereas SAA resided mostly in the amyloid cores. This differs from findings reported for ASC-Aβ colocalization, where ASC was found at the core of the plaque [15]. A graphical representation of the geolocation of the center of mass of pixels in space indicated a high distributional overlap between ASC and SAA (**Fig. S1B** and **S1C**). This provides evidence for the

113 colocalization of ASC and SAA in human cardiac tissue affected by inflammation-associated
114 amyloidosis.

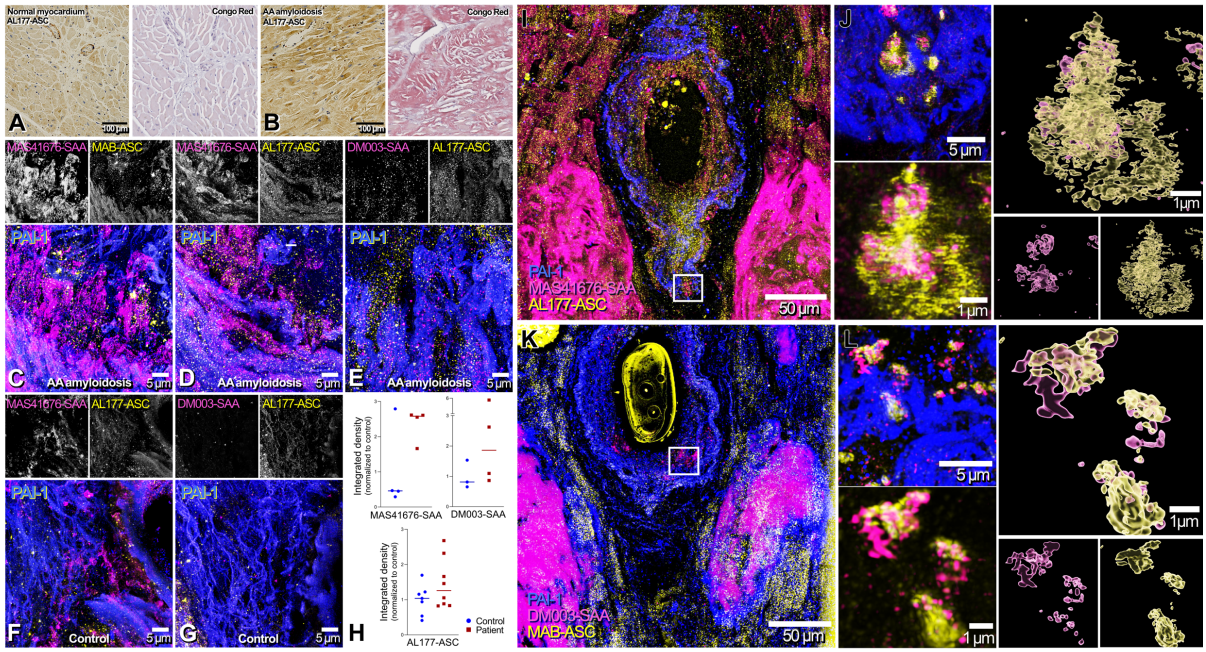

Fig. 1. Co-aggregation of ASC and SAA in human inflammation-associated AA amyloidosis. (A-B) ASC and Congo-red stained myocard from patients without (A) and with AA amyloidosis (B; 68 and 82-year old males, respectively) **(C-E)** Individual and merged confocal images of cardiac blood vessels (labeled with PAI1) from post-mortem tissue of patient with AA amyloidosis, presenting high level of SAA (labeled with MAS41676 and DM003) and ASC (labeled with AL177 and MAB/MY6745). **(F-G)** Individual and merged confocal images of cardiac blood vessels (labeled with PAI1) from post-mortem tissue, presenting low level of SAA (labeled with MAS41676 and DM003) and ASC (labeled with AL177). **(H)** Graphical representation of the quantification of 100X confocal images for SAA and ASC. Each point represents one field of view, bars represent median. Integrated density was normalized by the mean value control. We have refrained from performing a statistical analysis as we provide data from one patient in each group. **(I)** Confocal images from post-mortem tissue of patient with AA amyloidosis showing accumulation of both SAA (MAS41676, magenta) and ASC (AL177, yellow) within the blood vessel border (labeled with PAI1) and in adjacent muscle cells. **(J)** STED imaging of co-aggregation SAA (magenta) and ASC (yellow). Imaris 3D model shows the intricacy of SAA and ASC within these aggregates. **(K)** Confocal images from post-mortem tissue of patient with AA amyloidosis showing accumulation of both SAA (DM003, magenta) and ASC (MAB-ASC (MY6745), yellow) within the blood vessel border (labeled with PAI1) and in adjacent muscle cells. **(L)** STED imaging of co-aggregation of SAA (magenta) and ASC (yellow). Imaris 3D model shows the intricacy of SAA and ASC within these aggregates.

115

116 ***ASC specks interact with SAA through the pyrin domain to promote AA amyloid fibrillation***

117 The colocalization between ASC and SAA raises the question whether ASC may promote AA amyloid
118 formation. We therefore performed *in vitro* SAA aggregation assays. First, murine recombinant SAA
119 protein (mSAA1) and Thioflavin T (ThT) were incubated in the presence of ASC specks or of bovine
120 serum albumin (BSA) (**Fig. 2A**, upper panel). As we observed an accelerated amplification of mSAA1 in
121 the presence of ASC but not of BSA, we performed a dose-response experiment with 0-500k ASC specks
122 (**Fig. 2A**, lower panel). Data were fitted using a four-parametric logistic regression. We observed that

a higher number of ASC specks resulted in a left shift of the aggregation curve. In contrast, 500k ASC specks without mSAA did not induce any increase in ThT fluorescence (**Fig. 2A**, upper panel). To quantify the time at which the aggregation of murine SAA reached 50% of its plateau value (termed $t_{1/2}$), we performed global fitting using the AmyloFit software on each of the replicates individually. We found that $t_{1/2}$ was dose-dependently reduced by ASC specks, with higher doses leading to a significant reduction in $t_{1/2}$ (adjusted *p*: 0.013-0.048, Wilcoxon rank sum test with Holms correction for multiple comparisons, **Fig. 2B**). Hence the presence of ASC specks, but not of BSA, accelerates SAA fibril formation. To confirm direct interaction and to map the protein domains of interaction between ASC and SAA, we employed the limited proteolysis-coupled mass spectrometry (LiP-MS) technology [31-36] which detects changes in peptide cleavage exerted by limited proteinase K (PK)-based proteolysis by mass spectroscopy (MS) [37]. If an interaction between proteins exists, certain epitopes become inaccessible to PK and the peptides detected by MS will display an altered profile (**Fig. 2C**). First, we compared the $\log_2$ fold change of peptide representation of PK and trypsin-digested recombinant full-length ASC in the presence or absence of recombinant human SAA1 (**Fig. 2D**), with $|\log_2$ (fold change)$|>1$ and $-\log_{10}$(FDR-adjusted p-value) <0.05 as cutoffs for significance. Five significant changes in the ASC protein were identified (**Fig. 2D**, top, red color), all of which mapped to the pyrin domain of ASC and to part of the linker between pyrin and CARD domain (**Fig. 2D**, bottom), suggesting that this is the site where the protein-protein interaction with SAA occurs. The utilization of recombinant SAA1 fibrils instead of the monomeric form closely recapitulated the phenotype (**Fig. 2E**, top), but the linker site seemed to be more involved in the interaction (**Fig. 2E**, bottom). To validate the interaction between ASC and SAA1 also in a complex cellular background, we then incubated lysate of ASC-speck-producing ExpiHEK cells with recombinant human SAA1 and performed the LiP-MS workflow on control lysate and on lysate incubated with SAA1. Among all the interactors of SAA1 (419 LiP-MS hits) in ExpiHEK cells (**Fig. 2F**, blue points) we detected two peptides (red points) from the same region of ASC sequence. Although the altered peptides were slightly different from those of recombinant ASC, the pyrin domain (PYD) was again structurally changed, suggesting that it represents the site of interaction

149 with SAA1 (**Fig. 2F**). The PYD is also the site of interaction with Aβ [15], whereas the CARD domain is

150 known to interact with the CARD of Caspase-1 [38, 39].

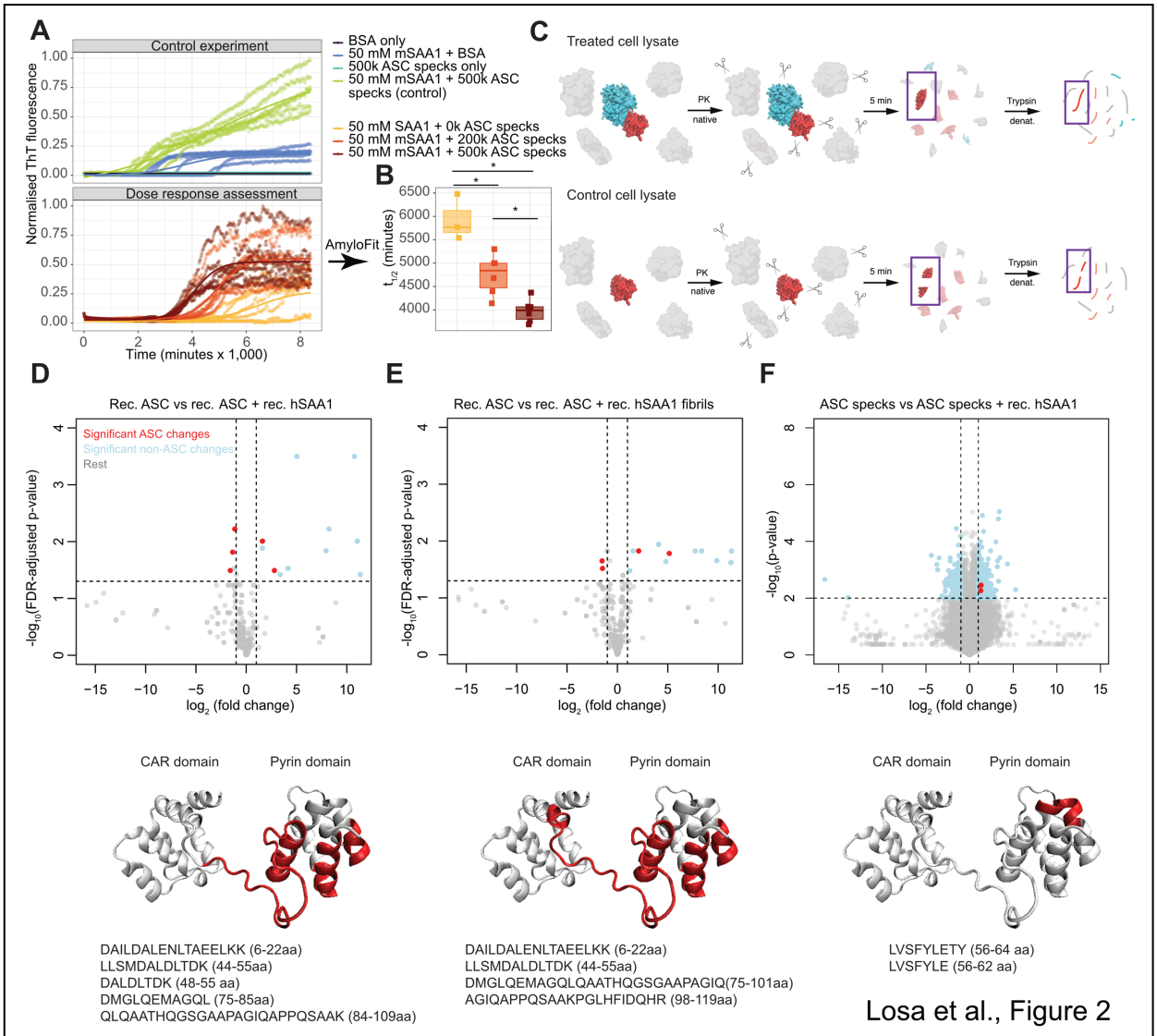

Fig. 2. ASC contacts specific SAA epitopes and accelerates SAA fibrillation. (A) *In vitro* SAA aggregation in the presence or absence of ASC specks over 150 hours. Each curve represents one technical replicate. **(B)** Latency to half-maximal fluorescence signal ($t_{1/2}$) for 0, 200k and 500k ASC specks. Boxplots: median and interquartile ranges (Wilcoxon rank sum test with Holm correction for multiple comparisons). Each dot represents one measurement. *: p<0.05. (**C**) Overview of LiP-MS. **(D-F)** Volcano plots (top) and ASC 3D structures (bottom) showing the affected epitopes (red) and respective amino acid sequences after mixing monomeric recombinant human ASC with monomeric recombinant human SAA1 (D), monomeric recombinant human ASC with recombinant human SAA1 fibrils (E), or human ASC specks with monomeric recombinant human SAA1 (F). Ordinate; FDR-adjusted (D-E) and unadjusted p-values (F); unpaired two-tailed t-test. In (D-F), the colours denote the following: Red – significant changes in the ASC protein. Light blue – significant changes other than in the ASC protein. Grey – rest, i.e. non-significant changes.

151

152 ***ASC does not modulate the induction of SAA by $AgNO_3$ or AEF***

153 We injected $AgNO_3$ and amyloid-enhancing factor (AEF), consisting of preformed AA fibrils, into 12

154 male and 10 female wild-type (*Pycard*$^{+/+}$), and into 14 male and 10 female B6.129-*Pycard*$^{tm1Vmd/tm1Vmd}$

(*Pycard*$^{-/-}$) littermate mice (**Fig. 3A**). Mice subjected to $AgNO_3$ and AEF injection were denominated "AA$^+$ mice". For control, mice were injected with either PBS, AEF, or $AgNO_3$ only. These mice were collectively denominated "AA$^-$ mice".

ASC might increase AA amyloid deposition by favoring its aggregation, or by enhancing SAA induction by inflammatory stimuli. Al^{3+}-containing adjuvants activate the NLRP3 inflammasome, but it is not known whether $AgNO_3$ stimulates ASC-dependent inflammasomes of innate immune cells [40], which would be a confounder in the current study. Thus, we assessed SAA levels of $AgNO_3$-only or AEF-only injected (i.e., AA$^-$) *Pycard*$^{+/+}$ and *Pycard*$^{-/-}$ mice by enzyme-linked immunosorbent assay (ELISA) and compared their SAA serum concentrations at baseline and up to 96 hours after injection. Serum concentrations of SAA and other acute-phase proteins peaked at approx. 24 hours after the proinflammatory stimulus (**Fig. 3B**). There was no significant difference in SAA serum concentration between *Pycard*$^{+/+}$ and *Pycard*$^{-/-}$ mice treated with only $AgNO_3$ or with only AEF at peak and at any of the time points investigated (Wilcoxon rank sum test, **Fig. 3B**). Hence, the genetic ablation of *Pycard* does not affect $AgNO_3$-induced SAA levels, suggesting that ASC-dependent inflammasomes do not significantly contribute to $AgNO_3$ sensing. Moreover, AEF alone was insufficient to induce serum SAA levels in an ASC-dependent manner. We deduce that the anti-amyloidogenic properties of ASC ablation is not due to a modulation of SAA induction.

$AgNO_3$-induced acute-phase responses in Pycard$^{-/-}$ and Pycard$^{+/+}$ mice

Having established the absence of a bias induced by $AgNO_3$ or with only AEF, we assessed SAA serum levels of *Pycard*$^{+/+}$ and *Pycard*$^{-/-}$ mice at baseline and 9, 24, 48, 72- and 96-hours post injection of $AgNO_3$ and AEF (i.e., AA$^+$) (**Fig. 3A**). There was a significant difference in SAA levels at 24 hours post injection (hpi) at the peak time of serum acute-phase protein levels [4, 41], between *Pycard*$^{+/+}$ and *Pycard*$^{-/-}$ AA$^+$ mice ($p = 0.004$, Wilcoxon rank sum test, **Fig. 3B**. At 0-9 hpi (hours post injection) there was no difference between mean SAA serum concentrations in *Pycard*$^{+/+}$ and *Pycard*$^{-/-}$ mice. However, at 24 hpi SAA serum levels of $AgNO_3$-treated *Pycard*$^{+/+}$ mice were significantly higher than in *Pycard*$^{+/+}$ mice

181 treated with $AgNO_3$+AEF (p = 0.03, Wilcoxon rank sum test). This suggests a "sink effect" by which SAA
182 is recruited by AEF and/or by nascent amyloid, and therefore decreases in serum. Crucially, this
183 reduction in SAA serum concentration did not occur in *Pycard*$^{-/-}$ AA^{+} mice. The mean SAA serum
184 concentrations of *Pycard*$^{-/-}$ AA^{+} mice were marginally higher than those of $AgNO_3$-only injected
185 *Pycard*$^{-/-}$ groups at 9, 24, 48 and 72 hpi, possibly because the ELISA detected some inoculated AA fibrils
186 that may still have been present in the bloodstream. At 48 hpi, SAA serum concentrations decreased
187 in all experimental groups. However, at this time point the difference between *Pycard*$^{+/+}$ and
188 *Pycard*$^{-/-}$ AA^{+} mice was still significant (p = 0.009, Wilcoxon rank sum test, **Fig. 3B**). Depending on the

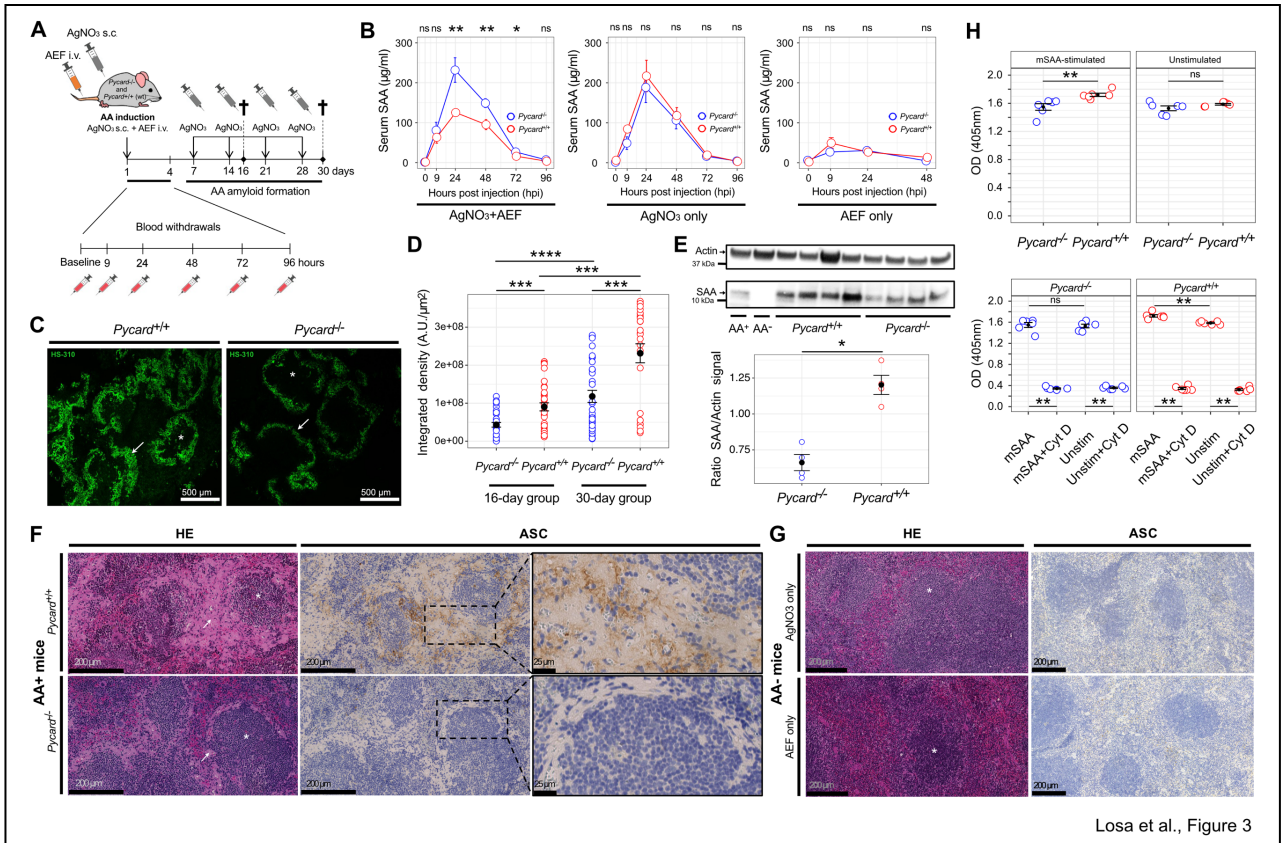

Fig. 3. Decreased splenic amyloid load in the absence of ASC. **(A)** Experimental design. **(B)** SAA serum concentrations (mean ± SEM; triplicates; Wilcoxon rank sum test) in *Pycard*$^{+/+}$ and *Pycard*$^{-/-}$ mice after injection of $AgNO_3$, AEF, or $AgNO_3$+AEF (AA amyloid induction). **(C)** AA^{+} (*Pycard*$^{+/+}$ and *Pycard*$^{-/-}$; P30) spleens stained with LCP (green). Arrows: red pulp invasion of amyloid. Asterisks: follicles. **(D)** Quantification of splenic LCP signal. Dots: individual mice. Scatterplots: mean ± SEM (error bars); Wilcoxon rank sum test with Holms correction for multiple comparisons. **(E)** Top: Western blot of monomeric SAA in spleen homogenates of *Pycard*$^{+/+}$ and *Pycard*$^{-/-}$ mice. Spleen homogenate from non-induced (AA^{-}) and AA^{+} C57BL/6 wt mice served as negative and positive control, respectively. Bottom: Quantification of Western blot data, from four mice per group. mean ± SEM; Kruskal-Wallis test. **(F)** Spleen sections stained with HE and ASC IHC from *Pycard*$^{+/+}$ (wt) and *Pycard*$^{-/-}$ AA^{+} mice. Arrows: amorphous amyloid structures. Asterisks: splenic follicles. ASC with brown stain in IHC. Boxes are magnified in the right panels. **(G)** Spleen sections stained with HE and ASC from *Pycard*$^{+/+}$ AA^{-} mice. **(H)** Phagocytic activity (OD) from unstimulated and mSAA-stimulated *Pycard*$^{+/+}$ and *Pycard*$^{-/-}$ BMDMs specimens. Each assay was carried out in duplicates. Cyt D: 10 µM Cytochalasin D. Mean ± SEM (error bars). Wilcoxon rank sum test with Holms correction for multiple comparisons. Dots: individual bone-marrow samples. * p<0.05, ** p<0.01, *** p<0.001, **** p<0.0001, ns: not significant.

189 genotype, the difference between SAA serum concentrations in *Pycard*$^{+/+}$ and *Pycard*$^{-/-}$ AA^{+} mice
190 persisted up to 72 hours after injections (p = 0.03, **Fig. 3B**). Finally, 96 hours after injection there was
191 no difference in SAA serum concentration. *Pycard*$^{-/-}$ AA^{+} mice were found to have the highest SAA
192 serum concentration among all experimental groups (**Table S2**). We conclude that ASC facilitates the
193 recruitment and deposition of SAA in murine inflammation-associated amyloidosis.
194
195 ***Decreased splenic amyloid deposition in the absence of ASC-dependent inflammasomes***
196 We assessed the presence of amyloid in spleens of mice with experimental AA amyloidosis (**Fig. 3A**) by
197 staining histological sections of paraffin-embedded tissue with Congo red (CR) (**Fig. S2**) and with the
198 luminescent conjugated polythiophene (LCP) HS-310 (**Fig. 3C** and **S3**). We sacrificed experimental
199 animals at day 16 or 30, two days after the last $AgNO_3$ injection. CR-stained amyloid showed the
200 characteristic red appearance in bright-field microscopy and apple-green birefringence under
201 polarized light, similarly to human myocardial tissue (**Fig. 1**). The red spleen pulp of *Pycard*$^{+/+}$ AA^{+} mice
202 exhibited more pronounced amyloid invasion than that of *Pycard*$^{-/-}$ AA^{+} mice (white arrows), and no CR
203 and LCP staining was detected in AA^{-} mice (**Fig. S2** and **S3**). The quantification of HS-310 fluorescence
204 intensity confirmed a significant difference in the amyloid load of *Pycard*$^{+/+}$ and *Pycard*$^{-/-}$ AA^{+} mice at
205 day 16 and 30 (adjusted p = 0.002 and 0.001, respectively; Wilcoxon rank sum test with Holms
206 correction for multiple comparisons) indicating that AA deposition is ASC-dependent (**Fig. 3D**). The
207 median difference increased over time from 2.3-fold (interquartile range (IQR): 0.8-2.7) at day 16 to
208 3.4-fold (IQR: 1.5-6.9) at day 30.
209 Using Western blot (WB), we assessed the presence of the AA amyloid precursor protein SAA in spleen
210 homogenate of the four *Pycard*$^{+/+}$ and *Pycard*$^{-/-}$ AA^{+} mice with the highest splenic amyloid load of the
211 30-days group (**Fig. 3E**). We observed a reduction of total splenic SAA in *Pycard*$^{-/-}$ AA^{+} mice. The median
212 reduction was 1.9-fold (IQR: 1.7-2.1). Like human AA aggregates, we found ASC immunoreactivity
213 adjacent to amyloid deposits (**Fig. 3F**). No amyloid or ASC signals were detected in AA^{-} mice of similar
214 age injected with either PBS, $AgNO_3$ or AEF (**Fig. 3G** and **S4**). ASC immunoreactivity was mostly detected

in the perifollicular region of *Pycard*$^{+/+}$ AA^{+} spleens (**Fig. 3F**). These data indicate that the AA amyloid load is strongly modulated by *Pycard*.

No specific transcriptional signature in macrophages upon amyloidosis induction

Prolonged elevation of serum SAA is required to trigger AA amyloidosis [42]. AA aggregates then progressively disrupt tissue integrity and ultimately impair the physiological function of affected organs. Furthermore, patients with systemic AA amyloidosis may exhibit altered red blood cell and platelet volumes [43, 44], which in turn can activate inflammasomes and boost the inflammasome capacity of macrophages, neutrophils and monocytes [45]. We therefore assessed the cellular composition of the spleen and of peripheral blood at baseline and after induction of experimental AA amyloidosis in *Pycard*$^{+/+}$ and *Pycard*$^{-/-}$ mice.

Using flow cytometry, we counted splenic B cells, T cells, dendritic cells, neutrophils as well as M1- and M2-like macrophages. Mice that had only been treated with $AgNO_3$ and AA^{+} mice showed increased splenic macrophage infiltration compared to baseline. Macrophage infiltration was neither dominated by M1- nor by M2-like macrophages (**Fig. S4**). We assessed the transcriptional state of fluorescence-activated cell sorted (FACS) splenic macrophages from *Pycard*$^{+/+}$ and *Pycard*$^{-/-}$ AA^{+} mice by RNA sequencing (**Fig. S5A** and **S5B**). Significant ($p < 0.05$; FDR < 0.01) transcriptional changes were only found in the *Pycard* gene, as expected, as well as in *Gdpd3* (**Fig. S5C** and **S5D**), a glycerophosphodiester phosphodiesterase of unknown relevance in the context of SAA. The absence of a distinct macrophage signature in inflammation-associated amyloidosis suggests that other inflammation-related proteins, such as cytokines, may not play an important role in AA formation and deposition.

Reduced phagocytic activity of SAA-activated Pycard$^{-/-}$ bone marrow-derived macrophages

Macrophages and monocytes play a central role in AA amyloidosis. They colocalize with AA amyloid in the spleen of AA^{+} mice [26] and can transfer AA amyloidosis *in vivo* [46]. Conversely, phagocyte depletion delays or inhibits AA amyloid accumulation [25, 29]. Moreover, AA amyloid undergoes Fcγ-receptor-

mediated phagocytosis by macrophages, which is initiated by host-specific antibodies that target the AA protein [30]. Since SAA activates macrophages [22-24], and *Pycard*$^{+/-}$ astrocytes of APP/PS1 transgenic mice overexpressing mutant amyloid β precursor protein and presenilin-1 (a mouse model of Alzheimer's disease) show increased Aβ phagocytosis [47], we investigated whether the presence or absence of ASC, in the context of SAA induction, influences the phagocytic activity of murine bone-marrow derived macrophages (BMDMs) *in vitro* (**Fig. S6A** and **S6B**). We exposed SAA-activated and non-SAA-activated murine BMDMs to an *in vitro* phagocytosis assay. There was no significant difference in phagocytic activity between unstimulated *Pycard*$^{+/+}$ and *Pycard*$^{-/-}$ BMDMs ($p = 0.4$, Kruskal-Wallis test) (**Fig. 3H**). However, activity was higher in SAA-stimulated than in unstimulated *Pycard*$^{+/+}$ BMDMs ($p = 0.002$) but not in SAA-stimulated compared with unstimulated *Pycard*$^{-/-}$ BMDMs ($p = 0.589$), suggesting that SAA is partially ASC-dependent in triggering phagocytosis. Furthermore, SAA-stimulated *Pycard*$^{+/+}$ BMDMs showed higher phagocytic activity than *Pycard*$^{-/-}$ BMDMs (p=0.002), underlining a functional implication of the ASC protein (**Table S4**).

We considered that the ablation of *Pycard* may cause pathologies of cellular compartments that do not require a direct ASC-SAA interaction. We assessed lymphocyte, monocyte, granulocyte, red blood cell and platelet counts in peripheral blood of AA^{+} and AA^{-} experimental animals (**Fig. S7** and **S8**). Of special interest were myeloid cells as well as platelets. The former form the cellular substrate of *Pycard*-dependent inflammasomes [48] whereas the latter were shown to be key for enhancing inflammasome activation and capacity of innate immune cells upon PRR stimulation [45]. Platelet count at baseline was higher in *Pycard*$^{-/-}$ than in *Pycard*$^{+/+}$ mice ($p = 0.017$). The same was observed for *Pycard*$^{-/-}$ AA+ mice from the 30-days group ($p = 0.036$, **Fig. S8**). The reduction of SAA-induced phagocytosis in *Pycard*$^{-/-}$ BMDMs (compared to *Pycard*$^{+/+}$ BMDMs) supports the notion that ASC is responsible for the modulation of AA amyloid deposition.

Anti-ASC immunotherapy diminishes inflammation-associated amyloid deposition

Therapeutic antibodies can interfere powerfully with amyloid formation [49]. We therefore asked whether treatment with anti-ASC antibodies can reduce AA amyloidogenesis in mice (**Fig. 4A**). We

generated a rabbit monoclonal anti-murine ASC antibody targeting the pyrin domain (PYD) and replaced its rabbit Fcγ domain with that of a mouse IgG_{2a} domain to avoid xenogeneic anti-drug responses in recipients and to improve its effector functions *in vivo*. The engineered antibody (denoted MY6745) showed high affinity binding to murine ASC^{PYD} (**Fig. S9A**). Purified, endotoxin-free mouse monoclonal anti-murine ASC and mouse monoclonal isotype control antibody were diluted in PBS to 2 mg/ml and intravenously injected (5 mg/kg body weight) at an interval of 7 days. Anti-ASC antibody serum levels were determined at various time points up to 96 hpi after the first injection and were found to peak at 24 hpi (**Fig. 4B**). Western blotting revealed that treatment of *Pycard*$^{+/+}$ AA^{+} mice with antibody MY6745, but not with a non-specific monoclonal isotype-control antibody, reduced total splenic SAA 2.3-fold (IQR: 1.7-3.0, $p = 0.01$, Kruskal-Wallis test, **Fig. 4C**). Following qualitative amyloid assessment on HE-stained sections (**Fig. 4D**) we performed ASC immunohistochemistry. The anti-ASC antibody treatment significantly diminished the ASC immunohistochemical signal in spleens of *Pycard*$^{+/+}$ AA^{+} mice (**Fig. 4E**), indicating effective target engagement and modulation. The groups significantly differed ($p = 9.9x10^{-5}$, Kruskal-Wallis test, **Fig. 4F**) and the median reduction was 2.7-fold (IQR: 2.4-4.8) compared to the untreated group (with 1.3-fold (IQR: 1.0-1.4) reduction for of the isotype-treated group). Following a quantitative assessment of mature extracellular amyloid, LCP-stained (**Fig. 4G**) spleen sections showed a conspicuous reduction in amyloid deposition of anti-ASC treated AA^{+} mice ($p = 0.007$, Kruskal-Wallis test, **Fig. 4H**). Importantly, anti-ASC antibody treatment had a strong effect, with a 2.5-fold (IQR: 2.4-3.3) reduction compared to the untreated condition, whereas the isotype-treated group only displayed a 1.2-fold (IQR: 1.1-1.7) reduction in amyloid deposition. Furthermore, AA^{+} mice treated with anti-ASC antibodies experienced a trend towards less severe loss of body weight than non-treated isotype-antibody injected AA^{+} mice, although the differences were not statistically significant (Kruskal-Wallis test, **Fig. S9B**). We conclude that anti-ASC treatment reduces AA amyloid deposition similarly to the ablation of *Pycard*.

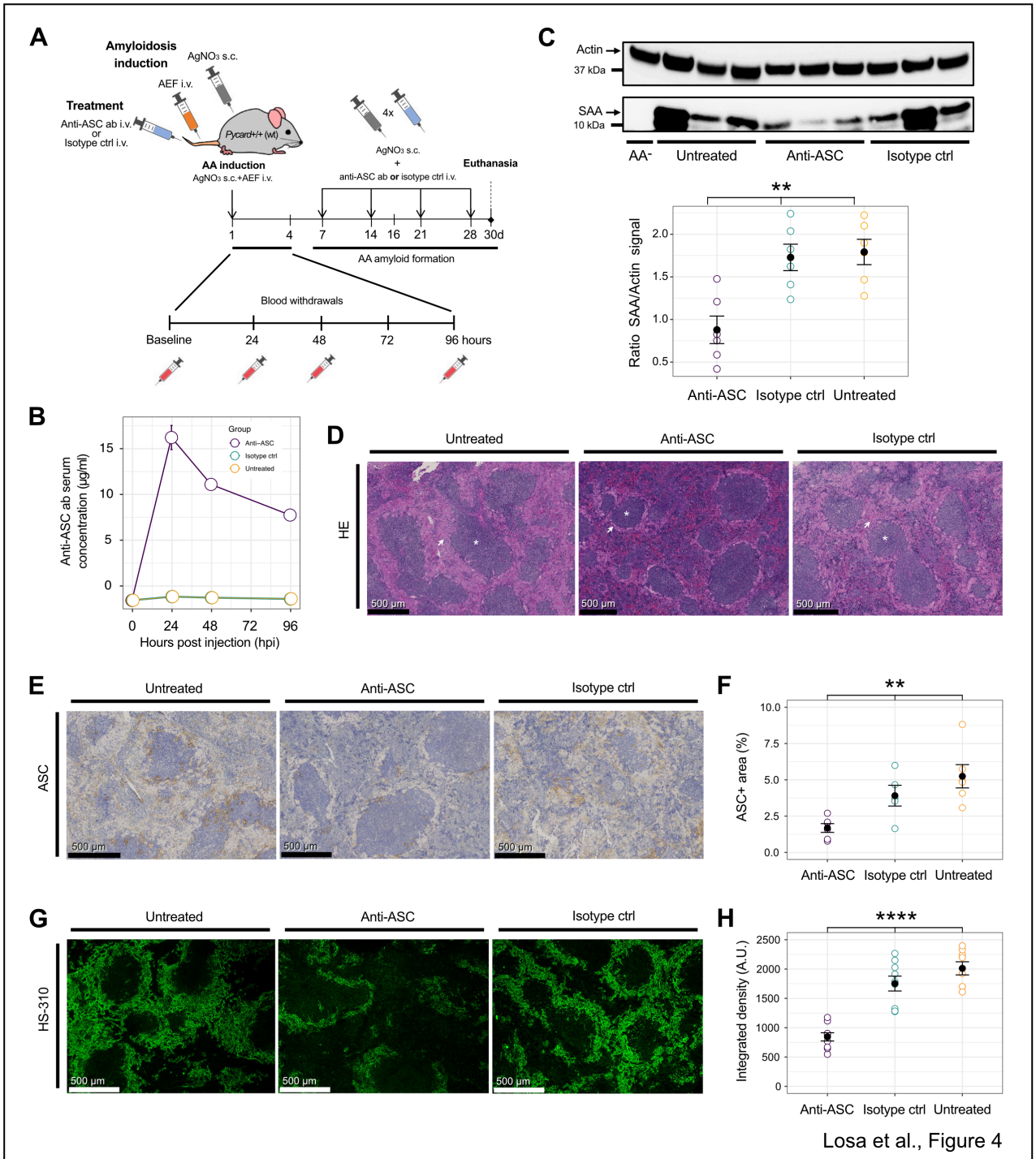

Fig. 4. **Anti-ASC immunotherapy reduces amyloid load**. **(A)** Scheme of anti-ASC immunotherapy. **(B)** Anti-ASC antibody single-injection pharmacokinetics. **(C)** Western blot of SAA in spleen homogenate of *Pycard*$^{+/+}$ AA^{+} mice treated with anti-ASC or isotype antibody, or untreated. Absence of amyloidosis induction as control (AA^{-}). Actin and spleen homogenate from a C57BL/6 wt mouse served as negative control. Scatterplots show data from three mice/group and two independent immunoblots (technical duplicates; mean ± SEM, Kruskal-Wallis test). **(D)** HE-stained spleen sections of *Pycard*$^{+/+}$ AA^{+} mice. Arrows: amyloid. Asterisks: white pulp. **(E)** Spleen sectiond stained with ASC antibodies (brown). **(F)** Quantification of ASC-positive areas in spleen sections. Two fields of view, each representing a different section for each mouse (3 mice/group) were quantified. Scatterplots: mean ± SEM. Statistics: Kruskal-Wallis test. **(G)** Spleen sections stained with LCP. **(H)** Integrated density expressed as arbitrary units/µm^2 in LCP-stained spleen sections. Each dot represents a quantified field of view. Three field of views for each animal were analyzed (nine fields of view from three mice per group). Scatterplots: mean ± SEM; Kruskal-Wallis test. * p<0.05, ** p<0.01, *** p<0.001, **** p<0.0001.

A large-scale investigation of anti-ASC autoantibodies in unselected hospital patients advocates stringent immune tolerance against ASC

Autoantibodies against aggregation-prone proteins can be beneficial against pathological protein aggregate but can also precipitate disease [50-52]. Having established that ASC controls the extent of amyloid deposition in inflammation-associated amyloidosis in mice and that ASC interacts with SAA via its PYD, we investigated whether natural anti-ASC antibodies exist in human antibody repertoires. Such autoantibodies could modulate systemic amyloidosis or conceivably other forms of protein aggregation. First, we established a high-throughput micro-ELISA using an automated robotic platform [53], using an ASC protein containing a C-terminal his-tag [15] at a concentration of 1 µg/ml at a well volume of 3 µl for coating. We then interrogated an unselected cohort consisting of 23,450 plasma samples from 19,334 patients admitted to various clinics at the University Hospital Zurich (**Fig. 5A**) for the presence of autoantibodies against monomeric ASC protein. The median age of the patients was 55 (interquartile range: 39-68) years and the female:male ratio was 47.3:52.7 (**Fig. 5B**). The largest fraction of samples originated from the department of cardiology, followed by dermatology, rheumatology, and hematology. We first compared the reactivity titers, i.e., the $-\log_{10}(EC_{50})$ or, in short, $p(EC_{50})$ values, of all patients with that of 119 patients with a history of amyloidosis based on ICD-10 code E85 ('Amyloidosis – excluding Alzheimer's disease'), including five individuals with AA amyloidosis, and with 21 patients with ICD-10 codes G30 or F00 ('Alzheimer's disease' and 'Dementia with Alzheimer's Disease'). None of the profiles protruded significantly from the collective (**Fig. 5C**, Kruskal-Wallis test with post-hoc Wilcoxon rank sum test). We then conducted an exploratory logistic regression analysis using a Bayesian LASSO [53, 54] on the entire dataset to identify whether, and which, ICD-10 codes are associated with seropositivity. At high specificity ($p(EC_{50})$ threshold value 2), the highest odds ratios were seen with ICD-10 codes E87 ('Other disorders of fluid, electrolyte and acid-base balance'), K58 ('irritable bowel syndrome'), and S69 ('Other and unspecified injuries of wrist and hand'). However, their odds ratios were 1.00 with 95% credible intervals of 0.78-1.61, indicating no effect. We additionally conducted a sensitivity analysis where we lowered the $p(EC_{50})$ cutoffs to 1.7

and 1.5, respectively. While lower cutoffs necessarily decrease the specificity of this analysis, we aimed to explore whether noteworthy differences would manifest more markedly. At p(EC_{50}) threshold value 1.7, the highest odds ratios were seen with ICD-10 codes J98 ('Other respiratory disorders'), E83 ('Disorders of mineral metabolism'), and R04 ('Haemorrhage from respiratory passages'). However, their odds ratios were 1.00 with 95% credible intervals of 0.86-1.64. Only when lowering the p(EC_{50}) threshold even further to values that cannot be considered biologically meaningful, some odds ratios started becoming different from 1.00. The three ICD-10 codes most associated with positivity were U99 ('Special screening examination for SARS-CoV-2'), K65 ('Peritonitis'), and E84 ('Cystic fibrosis), with odds ratios of 1.88, 1.33, and 1.31, respectively (see **Fig. S10**). However, these odds ratios entail large 95% credible intervals between 0.85 and 3.84. From this data exploration, we conclude that seropositivity at different cutoffs is not significantly associated with disease conditions.

By defining, based on previous studies [50], patients with p(EC_{50}) values ≥ 2 with respective fitting error < 20% as seropositive we identified five candidates who exceeded the threshold in the high-throughput screen (**Fig. 5C**, blue dots). The five seropositive candidates were then tested for specificity and reproducibility with an antigen panel. Only patient #5 confirmed reactivity against the ASC protein (**Fig. 5D**). The same patient did not show binding to control proteins such as the human recombinant prion protein (PrP_{23-230} or PrP), full-length tau (Tau441), or the natural Ara h 2 allergen but had received multiple SARS-CoV-2 vaccinations, which explains the positivity to the SARS-CoV-2 Spike protein. We then conducted an additional experiment on patient #5, to detail the epitope and account for potentially unspecific binding to the C-terminal his-tag on the ASC protein. Patient #5 displayed p(EC_{50}) values ≥ 2 against the full-length ASC protein as well as against the ASC CAR domain (CARD) but not against the ASC Pyrin Domain (PYD), or against his-tagged LAG3 or TIM3 control proteins (**Fig. 5E**). These results suggest that this patient, admitted to the hospital because of an acute relapsing tonsillitis, had elicited a genuine immune response targeting the CARD of the ASC protein. We conclude that the humoral response against the human monomeric ASC protein can indeed occur but is

344 exceedingly rare (< 0.01%). This indicates a stringent immune tolerance of the human immune system

345 to ASC.

346

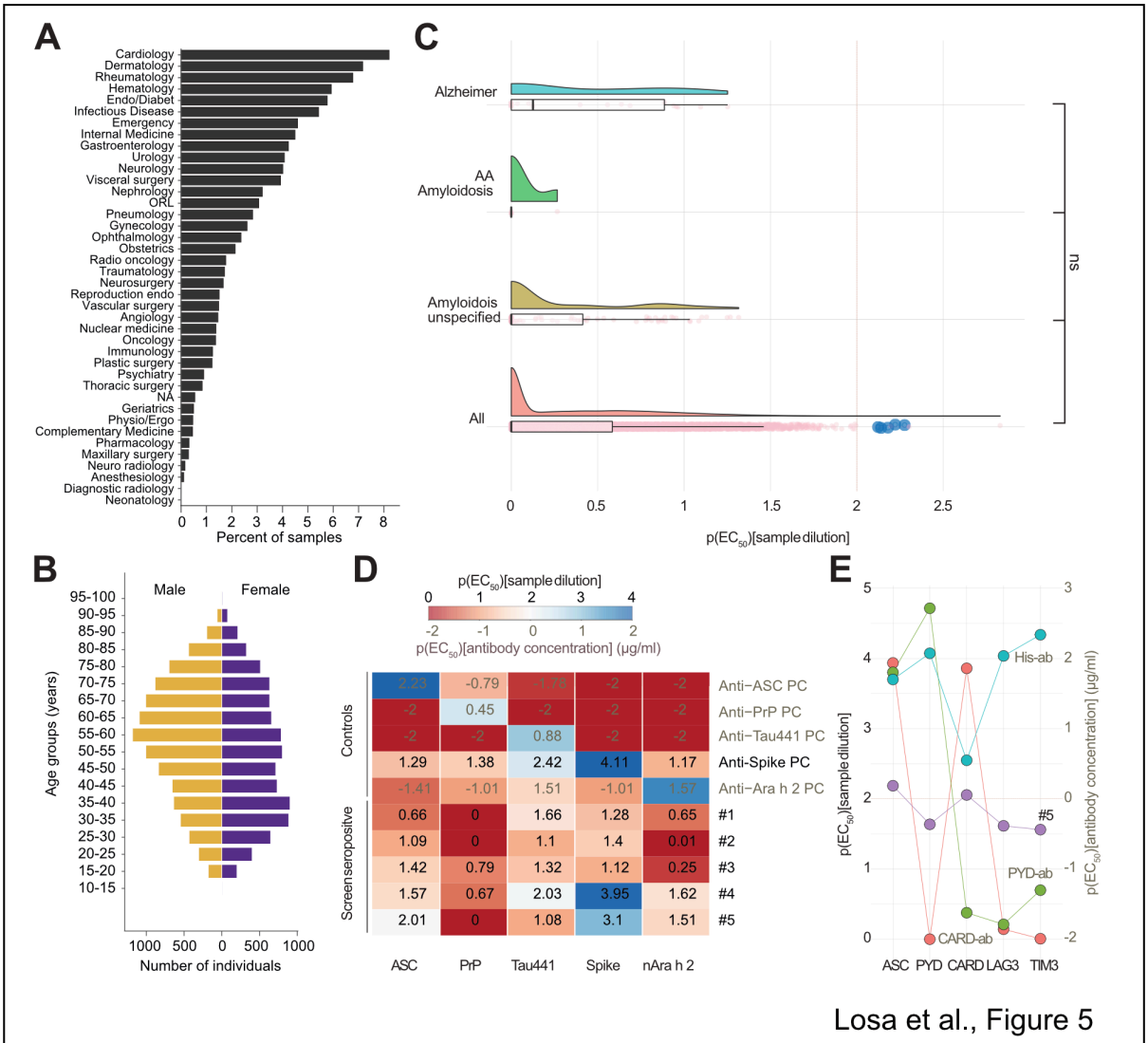

Losa et al., Figure 5

Fig. 5. **Population-wide interrogation of autoantibodies against ASC in a large unselected hospital cohort**. **(A)** Sample provenance by various hospital units. The contributions are depicted as percentage. **(B)** Age distribution of subjects. **(C)** Rainbow/boxplots displaying jittered p(EC_{50}) values for all patients screened (All), for the fraction of patients characterized by ICD-10 code E85 (Amyloidosis), AA amyloidosis, or Alzheimer's disease. Dashed red line at p(EC_{50}) = 2: reactivity cutoff. Blue dots represent the hits, characterized by p(EC_{50}) ≥ 2 and a mean squared residual error < 20% of the actual p(EC_{50}). None of the groups were significantly different (Kruskal-Wallis test *p*-value = 0.079, α = 0.01; Wilcoxon rank sum test *p*-value after Holm correction for multiple comparisons: 0.43 (All vs. Amyloidosis), 0.47 (All vs. AA Amyloidosis), 0.47 (Amyloidosis vs. AA Amyloidosis), 0.47 (All vs. Alzheimer), 0.28 (Amyloidosis vs. Alzheimer), 0.43 (AA Amyloidosis vs. Alzheimer), α = 0.01. **(D)** Heatmap showing p(EC_{50}) values of seropositive samples from screen and controls assayed against an array of antigens. Only the plasma of patient #5 exceeded the cutoff value and was a confirmed binder of human ASC. All samples and controls were assayed as duplicates. (e). Patient #5 (purple), along with multiple control antibodies, was assayed against the full-length ASC protein (ASC), the PY domain of ASC, the CAR domain of ASC, and against LAG3 and TIM3. All proteins used contained a his-tag. All samples and controls were assayed as duplicates. **(D-E)** Two scales are given: (1) For plasma samples, the p(EC_{50}) of the respective plasma dilution is used. (2) For monoclonal antibodies of known concentration, the p(EC_{50}) of the concentrations (in µg/ml) are shown. Anti-ASC, Anti-PrP, and Anti-Tau441 positive control (PC) as well as CARD-ab, PYD-ab, and His-ab are monoclonal antibodies.

Discussion

This study reports the co-aggregation of ASC, the central component of the NLRP3, NLRC4 and AIM2 inflammasomes [55, 56], with SAA in tissues of patients with inflammation-associated AA amyloidosis. The role of ASC in AA amyloidosis was investigated in a variety of experimental platforms including super resolution microscopy, AA fibrillization *in vitro*, limited-proteolysis mass spectrometry, and a murine model of inflammation-associated AA amyloidosis. In addition, we explored the potential of immunotherapy against ASC as a pharmacological approach for inflammation-related diseases, such as amyloidosis. Finally, we investigated the prevalence of naturally-ocurring anti-human ASC-autoantibodies on the population level. All the above studies indicate that ASC has a profound effect on the deposition of AA amyloid by interacting with SAA via its pyrin domain.

We used STED superresolution microscopy to investigate the topological relationship between ASC and SAA. In contrast with what was observed for amyloid β [15], we found that ASC co-aggregates in the periphery of AA amyloid. But does ASC physically interact with SAA, and if yes, through which epitope? Using an aggregation assay and LiP-MS, we found that the ASC-SAA interaction occurs at a few epitopes located in the pyrin domain of the ASC protein. This finding reflects the literature as the ASC pyrin domain, besides its well-known ASC-homodimerization characteristics [38, 57, 58], is described to be a protein interaction domain [15, 56]. Therefore, it is conceivable that the pyrin domain represents a potential target for therapy development. Since *in vivo* in *Pycard*$^{+/+}$ AA^{+} mice, the deposition of AA amyloid appeared to be more invasive into the red pulp than in *Pycard*$^{-/-}$ AA^{+} mice, we concluded that ASC inflammasome protein assemblies, driven by ASC^{PYD} oligomerization and ASC^{CARD} cross-linking, modulate amyloidogenesis or the deposition of AA amyloids in tissue, similarly to what has been shown for amyloid β [15] and tau [14] elsewhere. It is thus conceivable that ASC serves as a generic protein aggregation enhancing platform in various central and peripheral PMDs where the innate immune system is involved.

We probed alternative routes by which ASC could decrease the amyloid load. It is widely recognized that macrophages colocalize with amyloid deposits and that Fcγ-receptor-mediated phagocytosis plays

an important role in deposition, processing and clearing of AA amyloid [25, 26, 30, 59, 60]. We found that *Pycard*$^{+/+}$ murine BMDMs showed stronger phagocytosis than *Pycard*$^{-/-}$ BMDMs, similarly to phagocytosis of Aβ in a murine model of AD [47]. In addition, transcriptomic analysis of splenic macrophages of AA diseased mice revealed no significant differentially expressed genes between *Pycard*$^{+/+}$ and *Pycard*$^{-/-}$, and ASC transcripts were only identified in *Pycard*$^{+/+}$ mice, as expected, and there was an increased splenic macrophage infiltration in $AgNO_3$-only (AA^- mice) as well as AA^+ mice at the time of euthanasia, compared to baseline levels, which underscores the involvement of innate immune cells, especially myeloid cells, in the pathogenesis of AA amyloidosis. These findings suggest that the reduced splenic AA amyloid load in *Pycard*$^{-/-}$ mice is mainly due to the absence of ASC rather than enhanced phagocytosis of *Pycard*$^{-/-}$ BMDMs, even if there may be post-translational signatures or transcriptional changes that went unnoticed owing to limited sensitivity.

Another contributor to AA formation in chronic inflammation may be HDL-SAA complexes forming when entering the circulation. An *in vitro* ThT-fluorescence aggregation assay showed that HDL protects SAA from aggregation [61]. HDL may sequester SAA in an α-helical dominant conformational state, thereby preventing fibrillogenesis. Moreover, HDL-SAA complexes and monomeric SAA have been shown to be endocytosed into the lysosomal compartment of macrophages, where complex dissociation and self-assembly of SAA into AA protofibrils is initiated [61, 62]. ASC may therefore not only interact with SAA but also with HDL from the HDL-SAA complexes. This interaction may lead to SAA release from these complexes, shifting the equilibrium towards AA formation. Moreover, post-translational modifications such as phosphorylation and ubiquitination of ASC (CARD and PYD) regulate ASC assembly and inflammasome activity in a complex manner [63]. The sum of evidence, therefore, suggests that ASC-dependent acceleration of amyloidogenesis is due to physical amyloid scaffolding and/or to enhanced macrophage-dependent spread of seeds [24].

Having discovered that the ASC pyrin domain physically interacts with SAA, we hypothesized that a pharmacological targeting of this domain may recapitulate the results seen in the *Pycard* knockout model, i.e., reduced amyloid deposition. Indeed, anti-ASC^{PYD} antibodies were effective in reducing

399 amyloid load and may represent a viable therapeutic strategy. In this context, anti-ASC^{PYD} therapy
400 might impact the immune function indirectly path and might reduce the visceral AA amyloid load,
401 similarly to a combined therapy with small drugs targeting circulating serum amyloid P component
402 (SAP) and with a monoclonal anti-SAP antibody [60, 64].
403 Finally, in a population-wide anti-ASC autoantibody screen, performed in a cohort of cross-
404 departmental hospital patients, we investigated the humoral B cell response against the human
405 monomeric ASC protein. Any such anti-ASC autoantibodies could for instance neutralize ASC specks
406 that may also form neoepitopes. Consequently, the blockade of ASC could impair AA amyloid
407 formation. We observed that humoral response against ASC is exceedingly rare (< 0.01%), indicating a
408 high tolerance of the human immune system to ASC. Thus, natural anti-ASC autoantibodies are likely
409 not a key player in the modulation of inflammation-associated diseases such as amyloidosis.
410 Conversely, the absence of a natural immune response to ASC may increase the chance of high
411 tolerance as well as successful immunotherapy approaches employing anti-ASC antibodies in
412 inflammatory diseases. Moreover, higher -logEC_{50} values were not associated with any specific ICD-
413 coded diagnosis.
414 In conclusion, this study reports a crucial role for ASC in SAA interaction and recruitment, SAA serum
415 level modulation, SAA fibril formation acceleration, and controlling the extent of inflammation-
416 associated amyloidosis with respect to AA amyloid deposition. It is conceivable that the effect is not
417 only a result of the binding properties of ASC and ASC specks for β-sheet-rich proteins. Alternatively,
418 ASC assemblies may serve as aggregation-enhancing scaffolds in various PMDs. Finally, our findings
419 might have therapeutic implications that advance the fields PMDs and chronic inflammatory diseases
420 in general as ASC could be a target of disease-modifying therapies that aim to reduce amyloid
421 deposition and pathology in various proteinopathies.

Material and Methods

Histology and immunohistochemistry of human tissue

Formalin-fixed and paraffin-embedded cardiac sections (2-4 µm) were de-paraffinized with three cycles of xylene treatment followed by re-hydration with 100 % EtOH, 96 % EtOH, 70 % EtOH and water (each cycle 5 min) respectively. Hematoxylin and eosin (HE) as well as Congo red (CR) staining and ASC immunohistochemistry (IHC) were performed according to standard procedures used at our institute. IHC was performed with anti-ASC pAb (clone AL177, AdipoGen) at a dilution of 1:500.

For confocal and stimulated emission depletion (STED) microscopy, formalin-fixed and paraffin-embedded cardiac sections (15 µm) were de-paraffinized with xylene followed by re-hydration with 100 % EtOH, 95 % EtOH, 80% EtOH, 70 % EtOH and 50%EtOH. Sections were block with a 10% donkey serum, 5% BSA PBS 0.02% triton. PAI1 (PA1-9077, ThermoFisher), SAA (MAS-41676, Invitrogen), ASC (clone AL177, AdipoGen) and ASC (MY6745, Mabylon) were used at 1:200 dilution, SAA (DM003, OriGene Technologies) was used at 1:20 dilution, all in saturating buffer, for 48 h at 4 °C. Alexa 488, 568 and 647 from Invitrogen were used at 1:200 concentration in saturating buffer, for 24 h at 4 °C. Thioflavin S staining (1%) was performed for 15 min at room temperature. Sections were treated with Sudan Black before mounting in ProLong Diamond Antifade Mountant (ThermoFisher).

Confocal and super-resolution STED images were acquired on a Leica SP8 3D, 3-color gated STED laser scanning confocal microscope. 10x (NA 0.3, **Fig. S1**), 20x (immersion Oil, NA 0.75) and 100x (immersion oil, NA 1.4) images were acquired at a resolution of 2048x2048. 10x images were acquired with a 600Hz bidirectional scan yielding a XY resolution of 567.9um per pixel, 20x images were acquired with a 700Hz bidirectional scan yielding a XY resolution of 126.2 µm per pixel, and 100x images with a 1000Hz bidirectional scan yielding a XY resolution of 25.2 µm per pixel. Images were then deconvoluted using Huygens Professional software, and analyzed with image J Fiji. All presented images are max Z-projection and were adjusted for grey values identically for control and AA amyloidosis patient. STED images were visualized using Imaris 10.0.0 version.

Mice

Animal care and experimental protocols were in accordance with the Swiss Animal Protection Law and approved by the Veterinary office of the Canton of Zurich (permits ZH131-16 and ZH188/2020). Mice were bred in a high hygienic grade facility of the University Hospital of Zurich (BZL) and housed in groups of 2-5. Mice were under a 12-hour light/ 12-hour dark cycle (from 7 a.m. to 7 p.m.) at 21 ± 1°C. *Pycard*-deficient mice (B6.129-*Pycard*^{tm1Vmd}) were generated as previously published in Mariathasan, Newton, Monack, Vucic, French, Lee, Roose-Girma, Erickson and Dixit [55]. C57BL/6 wildtype mice were obtained from the Jackson laboratory. To minimize environmental bias and potential differences in microbiota, littermates were bred. We perfomed the experiments with highest possible gender and age congruence among experimental groups (**Table S5**-**S8**). Mice were randomly assigned to the experiments. In the anti-ASC antibody treatment experiment two mice in each of the antibody injected groups were found dead within the experiment.

Genotype screening

Ear biopsies were digested and subjected to PCR. An 859 bp *Pycard* allele fragment was amplified using forward 5'-GAAGCTGCTGACAGTGCAAC-3' and reverse 5'-CTCCAGGTCCATCACCAAGT-3' primers. Amplification of a 275 bp gDNA fragment from the B6.129-*Pycard*^{tm1Vmd} Neo cassette was done using forward 5'-TGGGACCAACAGACAATCGG-3' and reverse 5'-TGGATACTTTCTCGGCAGGAGC-3' primers. PCR products were run on a 1.5% agarose gel and developed for genotype definition.

AA induction and anti-ASC/isotype antibody injections

Silver nitrate (Merck) was eluted in nuclease-free water (Ambion®). AEF was prepared as previously described [65] and pH was adjusted to 7.4 before administration. AA amyloidosis induction was performed by injections of 100 µl AEF (i.v.) and 200 µl sterile filtered 1 % silver nitrate solution (s.c.) (Merck). Repeated injections of silver nitrate were in accordance with the reference [59]. To asses amyloid load and ASC distribution in *Pycard*$^{+/+}$ and *Pycard*$^{-/-}$ mice AA was induced in 22 *Pycard*$^{+/+}$ and 24 *Pycard*$^{-/-}$ mice, and 33 mice were injected with either PBS, $AgNO_3$ or AEF and served as controls (**Fig. 3A**). To perform the anti-ASC antibody treatment, a total of 15 Pycard$^{+/+}$ mice were induced with AA

($AgNO_3$ and AEF injections, i.e., AA^+) and additionally injected with either anti-murine ASC antibody or isotype control antibody (**Fig. 4A**). Anti-murine ASC and isotype control antibody were diluted in PBS with at a stock concentration of 2 mg/ml and intravenously injected at a concentation of 5 mg/kg bodyweight. Characteristics of experimental groups in **Table S5**-**S8**. Two mice of the antibody injected groups were found dead within the experiment and were therefore excluded from further analyses.

Mouse serum amyloid A (SAA) measurements

To determine the SAA levels in mice serum, blood was withdrawn into BD Microtainer® SST™ Tubes at baseline and up to 96 hours post injection. Samples were left at room temperature (RT) for 30 min and subjected to centrifugation at 10'000xg for 8 min at 4°C. Serum samples were then transferred and stored at -80°C. SAA levels were assessed by a mouse SAA enzyme-linked immunosorbent assay (ELISA) kit (abcam) according to the manufacturers' guidelines. Mouse serum samples were analyzed in technical triplicates. ELISA plate was developed and the optical density at 450 nm was measured.

Euthanasia and organ harvesting

Upon euthanasia, organs were harvested and kept on ice in Iscove's Modified Dulbecco's Medium (IMDM) (ThermoFisher Scientific) until measurement and further usage (no longer than 4 hours). Bone marrow cells of tibia, femur and pelvis were flushed into IMDM using 25G needles (B. Braun). Tissue was fixated in formalin for paraffin embedding or put in Tissue-Tek® O.C.T.™ compound (Sakura®) for frozen sections.

Histology and immunohistochemistry of murine tissue

Formalin-fixed and paraffin-embedded spleen or cardiac sections (2-4 µm) were de-paraffinized with three cycles of xylene treatment followed by re-hydration with 100 % EtOH, 96 % EtOH, 70 % EtOH and water (each cycle 5 min) respectively. Hematoxylin and eosin (HE) as well as Congo red (CR) staining and ASC immunohistochemistry (IHC) were performed according to standard procedures used at our institute. IHC was performed with anti-ASC pAb (clone AL177, AdipoGen) at a dilution of 1:500. To analyze the ASC-positive area (% of total area) the open-source software QuPath (https://qupath.github.io) was used. To perform LCP staining, slides were incubated with HS-310 for

30 min at RT in the dark at a final concentration of 0.3 µg/ml in PBS [66, 67]. After washing, slides were mounted with fluorescence mounting medium (Dako) and subjected to imaging on a fluorescence microscope (OLYMPUS BX61 fluorescence microscope system with an OLYMPUS XM10 camera). The hexameric LCP HS-310 was produced as previously described [68].

Fluorescence and polarized microscopy

To analyze LCP-stained tissue sections, we assessed three different and independent visual fields at 4x magnification and slides per mouse and organ. Two parameters, HS-310 positive area (% of area) as well as the fluorescence integrated density (A.U./µm^2) of HS-310 were calculated with the open-source software ImageJ (https://github.com/imagej/ImageJ). To confirm the presence of amyloid, we assessed the apple-green birefringence of amyloid under polarizing light in Congo red stained spleen tissue sections (**Fig. S2**). FACS sorted splenic macrophages were visually confirmed by filter settings that allowed the detection of PE-Cy5 and APC-Cy7.

SAA immunoblot analysis

To determine SAA presence by WB, spleen tissues from AA induced mice were homogenized in 1:9 volumes (w/v) RIPA buffer (50 mM Tris pH 7.4, 1 % NP-40, 0.25 % Deoxycholic acid sodium salt, 150 nM NaCl, 1 mM EGTA, protease inhibitors (complete Mini, Roche)) using TissueLyser LT for 45 seconds for four cycles. Samples were cooled on ice between cycles. Supernatant was transferred into new tubes after full speed centrifugation 16000g for 10 min at 4°C. Input (same volume per sample and blot) was boiled at 95°C for 10 min with a final concentration of 1 µM DTT and 4x NuPage™ LDS sample buffer (ThermoFisher Scientific). Spleen homogenate was separated using SDS-PAGE (Novex NuPAGE 4-12 % Bis-Tris Gels, Invitrogen) and transferred to a PVDF membrane (ThermoFisher Scientific) at 20 V for 7 min. Membrane was blocked with 5 % milk in TBS-T (Tris-Buffered Saline, 0.1 % TWEEN®20, pH 7.6) for 3 hours at RT. Primary rabbit anti-SAA antibody was incubated overnight (o/n) at 4°C at a concentration of 2.5 µg/ml (**Table S9**). Actin served as loading control. Membrane was incubated with primary mouse anti-actin antibody (Merck) at a 1:8000 dilution in blocking buffer at 4°C o/n. After 4 cycles of washing, membranes were incubated for 1 hour at RT with secondary horseradish peroxidase

(HRP)-conjugated goat anti-rabbit IgG (H+L) (Jackson Immuno) and with secondary HRP-conjugated goat anti-mouse IgG (H+L) (Jackson Immuno) diluted 1:5000 and 1:8000 in blocking buffer, respectively. Blots were developed using Luminata Crescendo Western HRP substrate (Milipore) and visualized with the Stella system (model 3200, Raytest) (**Fig. S11** and **S12**).

Production of monomeric ASC in E. coli

Monomeric human ASC-His, ASC-GFP-His and the ASC PYD domain (ASCPYD-His-SII) as well as the ASC CARD domain (ASCCARD-His-SII) were expressed in E. coli and purified from inclusion bodies via Nickel beads. Therefore, E. coli strain BL21(DE3) was transformed with pET-based vectors encoding the his-tagged ASC variants. Expression was done in self-inducing media (MagicMediaTM, Invitrogen) incubated at 37 °C for 1 h and 67 h at 20 °C. Subsequently, cells were harvested by centrifugation at 4000rpm for 30min. For cell lysis, the pellet was resuspended in 50 mM phosphate, 300 mM NaCl, pH 7.5 and sonicated on ice 10 min at 40% power (2 secpulse/pause). The suspension was then centrifuged at 14000g at 4°C for 30 min to collect the pellet containing the inclusion bodies. To solubilize the inclusion bodies, pellets were resuspended in 50 mM phosphate, 300 mM NaCl, 6 M Gua-HCl, 2 mM DTT, pH 7.5 for 30min at RT. Afterwards the suspension was centrifuged at 14000g at 4 °C for 30 min to remove residual insoluble cell debris. The supernatant was then incubated with Nickel beads (Themo, #88221) for 3 h at RT., The beads were washed once with 50 mM phosphate, 300 mM NaCl, 6 M Gua-HCl, 2 mM DTT, pH 7.5 and followed by 50 mM phosphate, 300 mM NaCl, 6 M Gua-HCl, 2 mM DTT, 20 mM imidazole pH 7.5. To elute the His-tagged proteins, beads were incubated with 50 mM phosphate, 300 mM NaCl, 6 M Gua-HCl, 2 mM DTT, 500 mM imidazole pH 7.5. The pH of the eluate was adjusted to pH 3.8 with diluted HCl. Next, the eluate was dialysed against 50 mM Glycine, 150 mM NaCl, pH 3.8 in 3500 Da cassette O/N at 4°C. To remove higher order aggregates, the dialysed samples were purified using a preparative SEC column (HiLoad 16/600 Superdex 75 pg). The monomeric proteins were finally concentrated using a VivaSpin 3000 Da column.

Production and purification of ASC specks

Untagged ASC specks were recombinantly produced similarly to what was previously described [69]. In brief, suspension HEK293 cells were transiently transfected with expression plasmids encoding full length human ASC or ASC-GFP using linear PEI 40 kDa. After 7 days of expression at 37 °C and 5% CO_2, cells were harvested and resuspended in Buffer A (320 mM sucrose, 20 mM HEPES-KOH (pH 7.5), 10 mM KCl, 1.5 mM MgCl2, 1 mM, EDTA, 1 mM EGTA. Cells were lysed by syringing (10x 20G, 20x 25G), freeze-thawing (3x), followed by subsequent syringing (20x 25G). Afterwards the lysate was centrifuged at 400g for 8 min, the pellet was resuspended in 2x CHAPS buffer (40 mM HEPES-KOH (pH 7.5), 10 mM MgCl2, 1 mM EGTA, 0.2 mM PMSF, 0.2 % CHAPS) and filtered using 5 µm centrifugal filters at 2000g for 10 min. The filtrate was then diluted and gently mixed with 1 volume of 2x CHAPS buffer and centrifuged at 2300g for 8 min. The resulting pellet was resuspended in 1 ml of 1x CHAPS buffer and centrifuged at 5000g for 8 min. This washing step was repeated twice. Afterwards the pellet was resuspended in 1x CHAPS buffer and loaded carefully on the top of 40% Percoll and centrifuged at 16000g for 10min. The interface layer containing the ASC speck particles was collected carefully and washed once by centrifugation at 5000g for 3 min and resuspension in 1X CHAPS buffer. Lastly, tag-free ASC specks were stained using an anti-ASC antibody and a fluorescently labelled secondary antibody. Antibody-stained fluorescent particles were quantified in a fluorescence microscope using a Bürker chamber, delivering absolute counts of ASC speck numbers.

ASC speck immunoblot analysis

To assess the purity and the presence of untagged ASC specks used in aggregation assays, purified protein or HEK cell lysate were boiled at 95°C for 10 min with a final concentration of 10 mM DTT diluted in NuPage™ LDS sample buffer (ThermoFisher Scientific). Proteins were separated using SDS-PAGE (Novex NuPAGE 4-12 % Bis-Tris Gels, Invitrogen) and transferred to a PVDF membrane (ThermoFisher Scientific) at 20 V for 7 min. Membrane was blocked with 5 % milk in TBS-T (Tris-Buffered Saline, 0.1 % TWEEN®20, pH 7.6) for 3 hours at RT. Primary rabbit anti-ASC antibody (clone AL177, AdipoGen) was incubated overnight (o/n) at 4°C at a dilution of 1:1000. After 4 cycles of

washing, membranes were incubated with secondary horseradish peroxidase (HRP)-conjugated goat anti-rabbit IgG (H+L) (Jackson Immuno) diluted 1:5000 in blocking buffer for 1 hour at RT. Blot was developed as described above (**Fig. S13**).

In vitro SAA fibril formation

Recombinant murine SAA1 was generated as previously described in [61]. The *in vitro* aggregation assay was carried out in a black 96-well plate (Greiner Bio-One, PS, F-bottom, black) on a FLUOstar OMEGA plate reader (BMG Labtech). SAA1 was dissolved in water to achieve a stock solution concentration of 10 mg/ml. The final reaction volume was 100 µl per well and consisted of 50 µM murine SAA1, 20 µM Thioflavin T (abcam) and 50 mM Tris buffer pH 8.0. ASC specks (quantified as described above) were diluted in PBS and added at various concentrations. Bovine serum albumin (BSA, Sigma-Aldrich) was dissolved in water to reach a final reaction concentration of 50 µM. The plate was agitated every 20 min by orbital shaking for 10 s at 100 rpm. The assay was performed at 37°C. Fluorescence (Ex: 450nm, Em: 490 nm) was measured over the course of 140 hours. We conducted two independent experiments (**Fig. 2A**). ThT fluorescence intensity values were displayed in the following manner: (1) We first transformed the data so that all conditions and repeats started with ThT fluorescence intensity 0 at timepoint 0 minutes. (2) We applied a range function separately onto both the control experiment as well as on the dose-response datasets, i.e.

$$\frac{x - \min(x)}{\max(x) - \min(x)}$$

where x was the adjusted ThT fluorescence intensity and min and max the respective minimum and maximum ThT fluorescence signals in each of the two experiments. This allowed us to obtain data scaled between 0 and 1 for the two datasets individually. The ordinate in **Fig. 2A** is therefore labelled as 'Normalised ThT fluorescence'. (3) To visualize trends over all replicates, we conducted four-parametric logistic regression analyses. (4) For quantification of $t_{1/2}$ values, data were fitted with a global fitting procedure using the software application AmyloFit according to the developer's instructions [70].

Limited proteolysis-coupled mass spectrometry (LiP-MS)

LiP-MS was conducted as shown earlier [31-35]. Briefly, we incubated purified recombinants ASC protein or ExpiHEK cell native lysates containing ASC specks with human recombinant SAA1 proteins for 15 min at 37 °C in LiP buffer (100 mM HEPES pH 7.4, 150 mM KCl, 1mM $MgCl_2$). Next, PK was added to each independent technical replicate simultaneously at 1:100 (w/w) enzyme to substrate ratio for 5 min at 37 °C. Four technical replicates per condition were done for purified proteins and three for ExpiHEK lysate. To stop limited proteolysis reaction, PK was heat-inactivated by sample incubation at 99 °C. Subsequently, samples were transferred into equal volume of 10% sodium deoxycholate (Sigma Aldrich). Next, samples were reduced with 5 mM tris (2-carboxyethyl)phosphine hydrochloride for 40 min at 37 °C under 800 rpm shaking, alkylated in 40 mM iodoacetamide, and incubated in the dark at RT for 30 min. Finally, samples were diluted in ammonium bicarbonate and digested with lysyl endopeptidase and trypsin (at enzyme to substrate ration of 1:100) at 37 °C for 17 h under 800 rpm shaking. Digestion was stopped by addition of formic acid (4% final concentration). Precipitate of sodium deoxycholate was removed via centrifugation, samples were desalted with Sep-Pak tC18 cartridges (Waters) and eluted with 80% acetonitrile, 0.1% formic acid. Samples were analyzed on an Orbitrap Fusion Lumos Tribrid mass spectrometer (Thermo Fisher) equipped with a nanoelectrospray ion source and an UPLC system (Waters) in data-independent acquisition mode. Spectronaut (Biognosys AG) software was used to search the raw MS data. The statistical data analysis was done in R. Two-tailed t test was applied to assess statistical significance between peptide abundances. Significance cutoffs of $|\log_2(\text{fold change})|>1$ and $-\log_{10}(\text{FDR-adjusted p-value}) <0.05$ or $|\log_2(\text{fold change})|>1$ and $-\log_{10}(\text{p-value}) <0.05$ were used, as indicated. LiP-MS hits corresponding to ASC protein were highlighted in red (**Fig. 2D-F**). Significant peptides originated from other proteins are depicted in blue. The blue data points in **Fig. 2D** and **2E** correspond to contaminants (i) originating from co-purified proteins. (ii) corresponds to SAA protein that was present only in one condition. We focused on significant changes in ASC protein (depicted in red).

626 *Differentiation of bone marrow cells to bone marrow derived macrophages (BMDMs)*

627 BMDMs were generated, with slight modifications, as previously published [71]. BM cells were harvested
628 from tibia and femur, washed twice in PBS, and resuspended in differentiation medium I-10 + M-CSF
629 (i.e., IMDM, 10 % FBS, 1 mg/ml Pen/Strep containing 25 ng/ml recombinant murine M-CSF
630 (PeproTech)) at a density of 1-2 Mio. cells/ml. After incubation for four days at 37°C differentiation
631 medium was exchanged. On day 8 attached BMDMs were detached using Accutase® (Innovative Cell
632 Technologies, Inc.), washed twice in PBS, counted, and used in the phagocytosis assay.

633 *Anti-ASC antibody cloning*

634 The anti-ASC antibody was cloned from B-cells of rabbits immunized with recombinant ASC (**Fig. 4B**).
635 Isotype control antibody is a similarly obtained anti-idiotypic rabbit monoclonal antibody isolated from
636 a rabbit immunized with a human IgG1 Fab. Recombinant antibodies were produced in a transient HEK
637 expression system and purified via protein A affinity purification on an automated AKTA system (AKTA
638 explorer FPLC, GE Healthcare). For *in vivo* studies rabbit V-regions were fused with murine constant of
639 mouse IgG2a heavy chain and kappa chain to minimize immunogenicity. Recombinant antibodies were
640 produced as described above but in addition remaining endotoxin was removed by hydrophobic
641 interaction chromatography (AKTA explorer FPLC, GE Healthcare). Endotoxin levels were measured
642 (Endosafe nexgen, Charles River) and only antibodies with less than 0.15 EU/mg were used for *in*
643 *vivo* studies.

644 *Anti-murine ASC antibody binding assay*

645 High-binding clear flat bottom 384-well plate (Huber lab) were coated o/n (4°C) with 10 µl/well of
646 murine ASC (Cusabio, CSB-EP861664 MO) at a concentration of 1.25 µg/ml or BSA at a concentration
647 of 1 µg/ml diluted in PBS. After o/n incubation, wells were aspirated and washed once with 100 µl/well
648 of wash buffer (0.05% Tween®20 in PBS). Wells were blocked for an hour with 50 µl of 2% BSA diluted
649 in PBS at RT. After blocking, wells were incubated 2 hours at RT with 10 µl of test antibody (anti-ASC
650 or isotype ctrl) and serially diluted. Wells were washed four times and consecutively incubated with
651 10 µl/well of detection antibody for an hour at RT. Unbound detection antibody was removed by

washing four times, and the wells were incubated with 20 µl TMB for 5 min. The reaction was stopped by adding 10 µl of 1 M H_2SO_4 per well. Absorbance was immediately read at 450 nm.

Anti-ASC antibody serum concentration measurements

Serum was isolated as previously described. 384-well SpectraPlate HB plate was coated with recombinant ASC-his at a concentration of 1 µg/ml in PBS (pH 7.4) and incubated o/n (4°C) with 20 µl/well. Plates were then washed three times with sample buffer (0.1% Tween®20 in PBS) and blocked with blocking buffer (5 % SureBlockTM (Lubio Science, #SB232010-250G) in sample buffer) for 90 min at RT. Blocking buffer was removed by plate flipping. Murine serum samples as well as positive (anti-ASC monoclonal ab, Mabylon AG) and negative (isotype control ab, Mabylon AG) assay controls were resuspended in sample buffer followed by serial dilution and incubation for 2 hours at 37°C. Starting concentration of anti-ASC mAb was 2 µg/ml. Starting dilution of mouse serum samples was 1:20. After four wash cycles, HRP-conjugated secondary antibody (Goat anti-mouse IgG (H+L), Jackson ImmunoResearch, #115-035-003) were incubated for 1 h, at RT at a dilution of 1:4000 (in sample buffer). After three wash cycles, plate was developed with 20 µl/well TMB and incubated for 5 min at RT in the dark. Reaction was stopped with 20 µl/well 0.5 M H_2SO_4. Finally, absorbance was read at λ = 450 nm using an EnVision plate reader (Perkin Elmer). Serum samples as well as controls were assayed in technical duplicates.

In vitro phagocytosis

The phagocytosis of BMDMs was performed using a phagocytosis assay kit (abcam). Individual samples were prepared in duplicates. The in *vitro* assay was performed in 96-well tissue culture plates (TPP). *Pycard*$^{+/+}$ and *Pycard*$^{-/-}$ BMDMs were suspended at a density of 500'000 cells/ml. BMDMs were stimulated, with slight modifications, as previously published [23]. BMDMs were stimulated with murine SAA1 at a concentration of 2 µg/ml for 16 hours at 37°C prior to phagocytosis substrate encounter. After 1-hour phagocytosis substrate incubation at 37°C, cells were treated according to the manufacturer's guidelines and proceeded to EnVision Multimode Plate Reader (PerkinElmer) for data acquisition. The absorbance was determined at 405 nm.

Assessment of cellular spleen composition by flow cytometry

After sacrifice, cells were isolated from spleens using a 70 µm cell strainer (Falcon®). Following red blood cell lysis, cells were stained with the following monoclonal antibodies to determine cellular architecture of most abundant spleen and immune cells (**Table S10**): anti-mouse CD45.2 (Biolegend), anti-mouse Gr-1 (eBioscience), anti-mouse F4/80 (eBioscience), anti-mouse CD11b (Biolgegend), anti-mouse B220 (Biolegend), anti-mouse CD3 (Biolegend), anti-mouse CD206 (Biolegend), anti-mouse MHCII (Biolegend) and anti-mouse CD11b (eBioscience). Data acquisition and analysis was performed on a BD LSRIIFortessa™ flow cytometer and FlowJo v10.6.1, respectively. Gating strategy was applied, with slight modifications, as previously published [72-74].

RNA extraction and high-throughput sequencing (NGS)

Upon flow cytometric sorting of F4/80+/CD11b+ splenic macrophages originating from AA^+ mice (see above) total RNA was extracted using TRIzol™ Reagent (ThermoFisher Scientific) according to the manufacturer's guidelines and proceeded to high throughput sequencing (NGS). RNA integrity and quantity were assessed by RNA ScreenTape Analysis (Agilent). The SMARTer Stranded Total RNA-Seq Kit- Pico Input Mammalian (Takara) together with a NovaSeq platform (Illumina) was applied for transcriptomic data acquisition. Data was analyzed using established analysis pipelines at the Functional Genomics Center Zurich (FGCZ).

Complete blood count (CBC) from peripheral blood

Blood was withdrawn into Microvette® 100 K3E (SARSTEDT Germany) cuvettes according to the manufacturer's guidelines. To assess CBCs, samples were run on an ADVIA (Siemens Healthineers) hematology system.

Experimentation with human samples

All experiments and analyses involving samples from human donors were conducted with the approval of the ethics committee of the Canton Zurich (KEK-ZH-Nr. 2015-0561, BASEC-Nr. 2018-01042, and BASEC-Nr. 2022-00293) and in accordance with the provisions of the Declaration of Helsinki and the Good Clinical Practice guidelines of the International Conference on Harmonization.

High-throughput antibody profiling in unselected patient cohort and validation experiments

Serological screens were conducted as shown [50, 75, 76]. Briefly, high-binding 1536-well plates (Perkin Elmer, SpectraPlate 1536 HB) were coated with 1 µg/ml human ASC protein containing a C-terminal his-tag in PBS at 37 °C for 1 h, followed by three washes with PBS-T and by blocking with 5% milk in PBS-T for 1.5 h. Three microliter plasma, diluted in 57 µl sample buffer (1% milk in PBS-T), were dispensed at various volumes into human ASC-coated 1,536-well plates using contactless dispensing with an ECHO 555 Acoustic Dispenser (Labcyte). Thereby, dilution curves ranging from plasma dilutions 1:50 to 1:6,000 were generated (eight dilution points per patient plasma sample). After the sample incubation for 2 hours at RT, the wells were washed five times with wash buffer and the presence of IgGs bound to ASC were detected using an HRP-linked anti-human IgG antibody (Peroxidase AffiniPure Goat Anti-Human IgG, Fcγ Fragment Specific, Jackson, 109-035-098, at 1:4,000 dilution in sample buffer). The incubation of the secondary antibody for one hour at RT was followed by three washes with PBS-T, the addition of TMB, an incubation of three minutes at RT, and the addition of 0.5 M H_2SO_4. The well volume for each step reached a final of 3 µl. The plates were centrifuged after all dispensing steps, except for the addition of TMB. The absorbance at 450 nm was measured in a plate reader (Perkin Elmer, EnVision) and the inflection points of the sigmoidal binding curves were determined using a custom designed fitting algorithm. Samples reaching half-maximum saturation (shown as the inflection point of the logistic regression curve) at a concentration ≤ 1:100, i.e., at $p(EC_{50}) \geq 2$, and with a mean squared residual error < 20% of the actual $p(EC_{50})$ were considered hits. The inclusion of a threshold for fitting error ensures a reliable identification of positives from high-throughput screening. Negative $p(EC_{50})$ values, reflecting nonreactive samples, were rescaled as zero.

For the validation screen, hits from the high-throughput screen were tested against a panel of antigens consisting of recombinant human ASC protein, human $recPrP_{23-230}$, the full-length tau protein (Tau441), the SARS-CoV-2 Spike ectodomain and natural Ara h 2 allergen. The validation screen was performed identically to the primary high-throughput screen, except that duplicates were used instead of unicates and a 384-well plate format was chosen. Samples from the validation screen were considered

confirmed if p(EC_{50}) for PrP ≥ 2 (distinct reactivity against ASC) and p(EC_{50}) for other targets < 2 (no distinct reactivity against any other control target), except for the SARS-CoV-2 Spike protein, which was included to assess potential associations with acute infection or vaccination. The following assay positive controls were used at a starting concentration of 1 µg/ml: (1) Anti-ASC/TMS1/PYCARD Antibody (B-3) mouse monoclonal IgG1 (sc-514414, Santa Cruz); (2) anti-human PrP antibody huPOM1 [50]; (3) Anti-Tau (4-repeat isoform RD4) Antibody, clone 1E1/A6 (05-804, Sigma-Aldrich). Additional assay positive controls used at a starting dilution of 1:50 were: a plasma pool of patients admitted to the University Hospital of Zurich due to COVID-19 (anti-Spike PC); plasma of a patient identified to be seropositive for IgG against nAra h 2 (anti-Ara h 2 PC). The experiment on the two ASC domains (PYD and CARD, both of them containing a C-terminal his-tag; produced by Mabylon AG, Schlieren) and on additional his-tagged proteins as controls (his-LAG3 [77], his-TIM3 (AcroBiosystems)) was conducted using the same ELISA protocols as outlined above. Antigens and antibodies used for the high-throughput antibody profiling are shown in **Table S11** and **S12**.

Statistical analysis

Statistical analysis was performed using GraphPad Prism v9, Python3 and R. If not indicated otherwise, we conducted Kruskal-Wallis test with post-hoc Wilcoxon rank sum test with Holms correction for multiple comparison on non-parametric data. Statistical details are described in the respective figure legends and in the Result section. A two-tailed *p*-value <0.05 was considered as statistically significant in all group-based experiments, except for the exploratory ICD-10 code-based analysis where the significant threshold, α, was 0.01. Confidence intervals were calculated at a confidence level of 95 %. When reporting medians, we usually provided the interquartile range (IQR). Human data are stored in an *MS-SQL* database. Multiple regression with a logit link function using various p(EC_{50}) cutoff values for ICD-10 data exploration was performed using the rstanarm package (https://mc-stan.org/rstanarm/) with a Bayesian LASSO prior, similar to what was expounded in detail previously [53, 54].

Acknowledgments

We appreciate that Dr. Emmanuel Contassot shared the B6.129-*Pycard*^{tm1Vmd} mice. We thank Dr. Marcus Fändrich and his colleagues for providing murine SAA1 protein. We are grateful that Dr. Itzel Condado-Morales and Dr. Sathish Kumar provided technical support with the aggregation assay and data analysis. We thank Dr. Markus Manz that we could use the ADVIA hematology system. We thank Inga Hochheiser and Dr. Matthias Geyer (ISB, University of Bonn, Germany) for providing the human ASC and the team of Mabylon AG (Schlieren) for sharing the ASC-PYD and the ASC-CARD proteins. We thank Petra Schwarz, Rita Moos, Jingjing Guo, Mirzet Delic and Paulina Pawlak for their valuable technical knowledge, advice and assistance in mouse breeding and experimental injections. We thank the histology team at the institute for neuropathology for their support. We thank the RNA sequencing core from the University of Zurich for their help in the data analysis. The high-throughput antibody profiling-related work was funded through an SPHN driver grant (2017DRI1) and through NOMIS Foundation, the Schwyzer Winiker Stiftung, and the Baugarten Stiftung (coordinated by the USZ Foundation, USZF27101) awarded to AA and ME. AA is supported by the Swiss National Science Foundation (grant # 179040) and the NOMIS Foundation.

Statement of author contribution

Initiated, conceptualization and lead the project: ML, AA. Conceived and designed the experiments: ML. Supervised the project: AA. Wrote the ethical applications to perform the animal experiments: ML, AKKL. Wrote the ethical applications to perform experiments with human samples or data: ME, RRR. Animal breeding and genotyping: ML. Performed *in vivo* experiments: ML, PMS. Anti-ASC antibody cloning, expression, and purification: NP, DC, DB. Animal injections: ML. Performed the *in vitro* as well as human HTS confirmatory experiments: ML, ME, TS, SH. Bulk RNA isolation: ML, MC. Isolated and purified murine AEF: GTW. Synthetized and purified LCP: KPRN. Histology: ML, PDR, ME. Provided human autopsy material: NJR. Contributed reagents and materials: KJF, MN. Flow cytometry and FACS experiments: ML, VL, PMS. Analysis and visualization of the data: ML, ME, PDR, PMS. Conducted the

782 population-wide anti-ASC autoantibody screen and profiling: ME. Wrote the original draft of the
783 manuscript: ML, ME. Edited manuscript: ML, ME, PDR, AA, PMS, NP, TS. Approved manuscript: all
784 authors.

785

786 **Data and material statement**

787 Primary data and reagents will be shared and made available upon request. Antibodies against ASC are
788 the property of Mabylon AG and will be shared upon reasonable request under specific material
789 transfer agreement terms.

790

791 **Declaration of interests**

792 AA is a founder, shareholder, director, and consultant for Mabylon AG, which has developed the anti-
793 ASC monoclonal antibody used in this study. NP, DC, DB are employees of Mabylon AG.

794

Supplemental figures

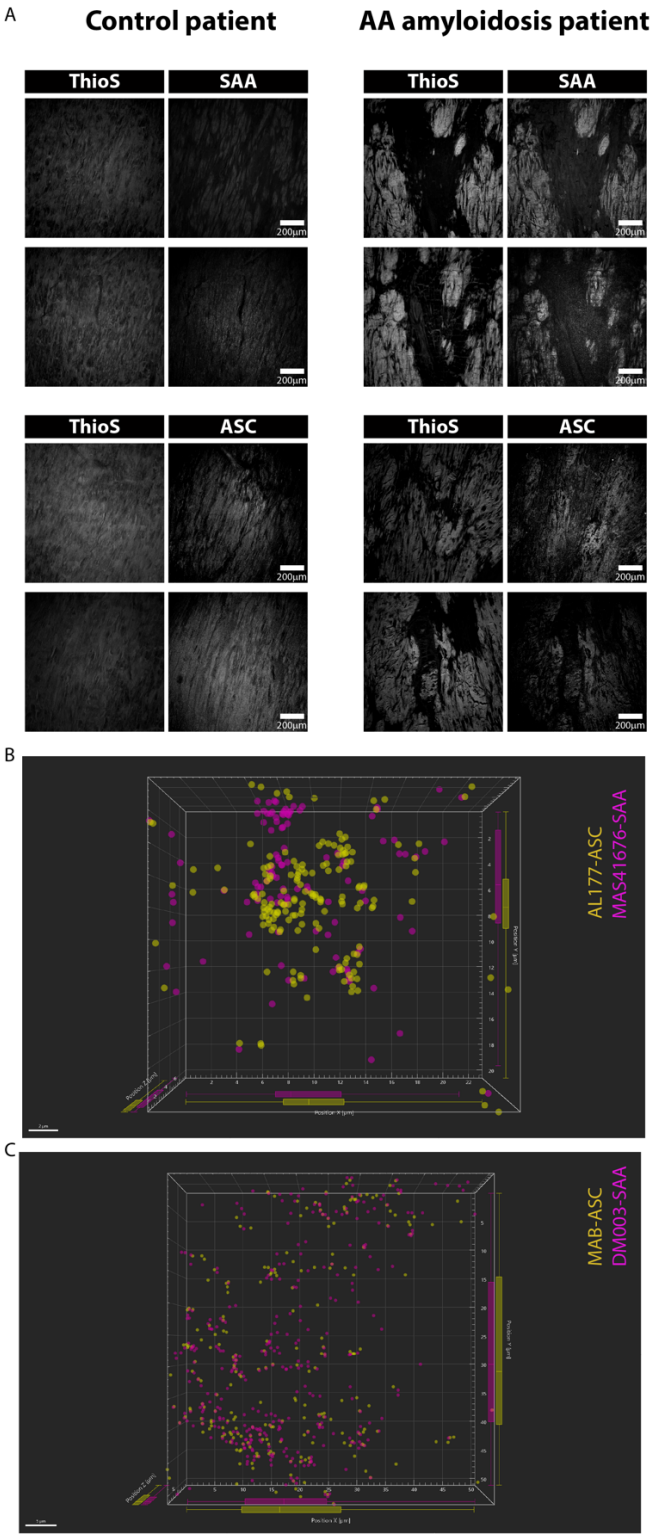

Fig. S1. Colocalization of Thioflavin S staining with ASC and SAA and 3D representation of ASC and SAA staining. (A) Confocal images of patient with or without AA amyloidosis showing Thioflavin S staining, revealing protein aggregates forming β-sheets, and SAA or ASC. All grey levels were adjusted identically for both subjects. **(B)** and **(C)** Plot presenting 3D geolocalisation of center of mass of the dots reconstructed on the STED signal for ASC and SAA. On the side, boxplots represent the distribution in X, Y, and Z direction. The distributions of ASC and SAA are highly congruent.

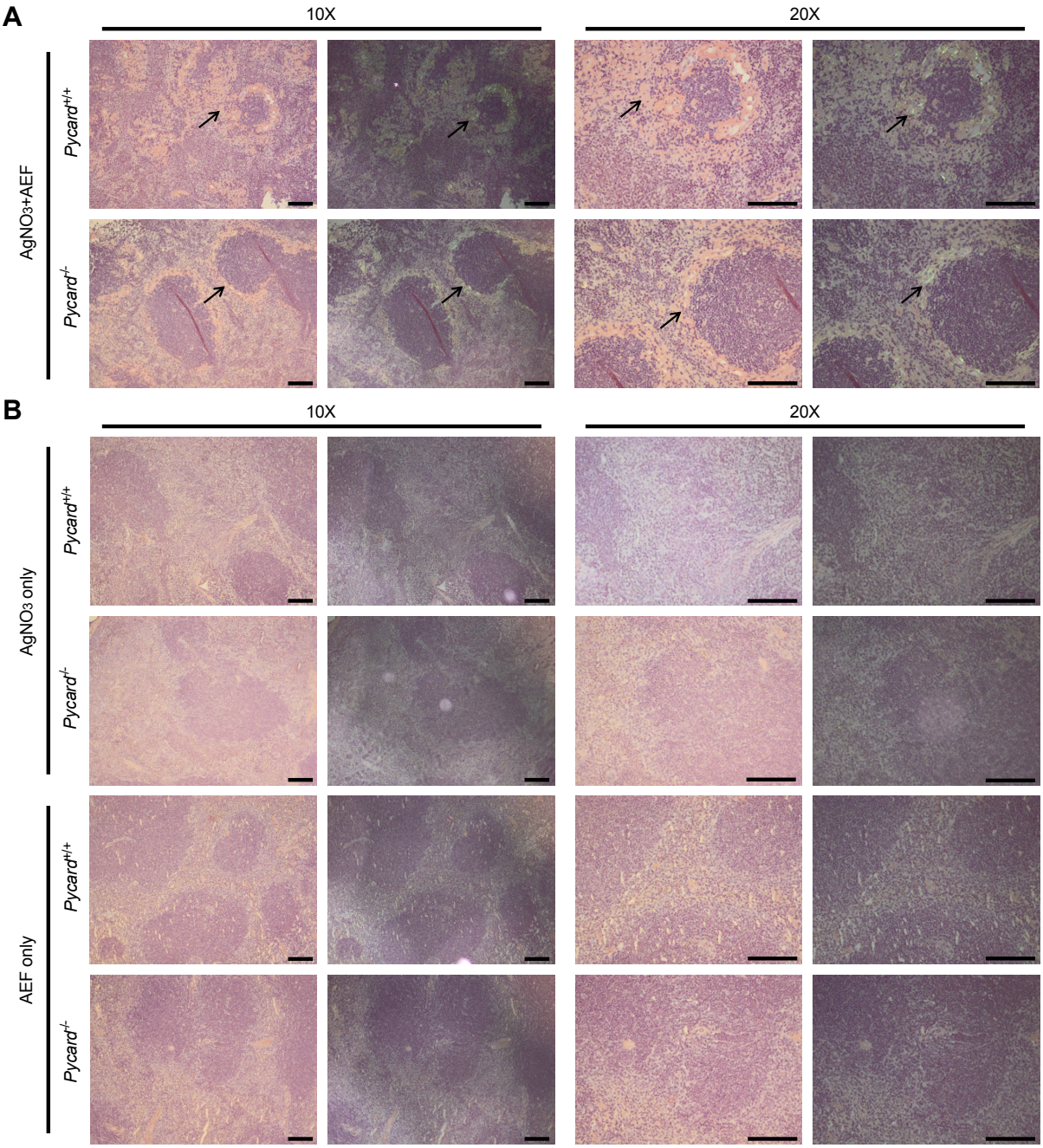

802

803 **Fig. S2**. **Amyloid stained by Congo red shows apple-green birefringence in polarized light only in mice with AA induction**.
804 **(A)** Representative Congo red-stained photo micrographs from indicated experimental groups showing amyloid apple-green
805 birefringence (black arrows) under polarized light in AA^{+} mice that received both, AEF and $AgNO_3$ injections [78]. In light
806 microscopy, amyloid manifests as amorphous pink material (black arrows). **(B)** Important to note, there is no amyloid in the
807 $AgNO_3$ only nor in the AEF only treated group (AA^{-} mice). Scale bar 100 µm.

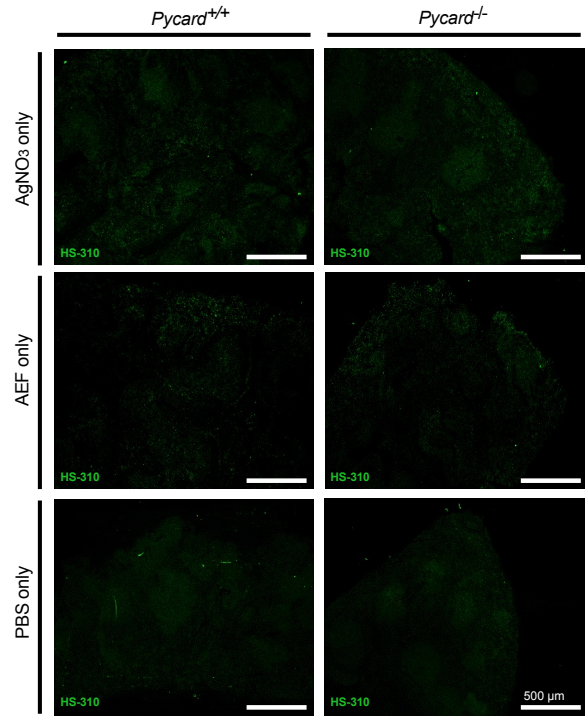

Fig. S3. **Absence of amyloid deposition in mice only treated with $AgNO_3$, AEF or PBS (AA^- mice)**. Visualization of amyloid deposition by hexameric LCP HS-310. No amyloid was seen in the control groups ($AgNO_3$-only, AEF-only and PBS-only). Light exposure time and 4x microscope objective were kept equal throughout the imaging/experiment.

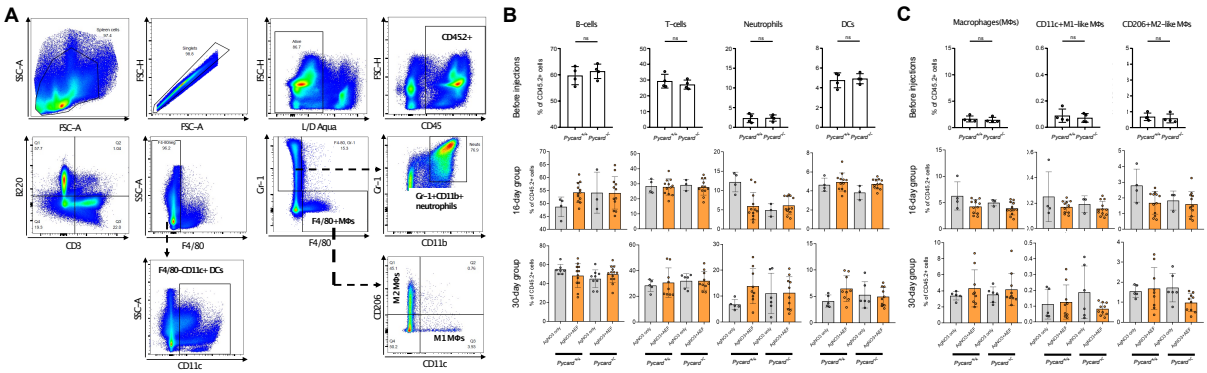

Fig. S4. **Assessment of splenic cellular architecture before injections and AA disease state**. **(A)** Representative flow cytometry analysis and gating strategy of murine spleen cells. CD45.2 is an alloantigen expressed on all hematopoietic cells (except mature erythrocytes and platelets). B cells defined as CD45+CD3-B220+, T cells defined as CD45+B220-CD3+, Dendritic cells (DCs) defined as CD45+F4/80-CD11c+ and Neutrophils defined as CD45+Gr-1+CD11b+. Macrophages (MΦs) defined as CD45+F4/80+, and M1-like MΦs defined as CD45+F4/80+CD206-CD11c+ whereas M2-like MΦs defined as CD45+F4/80+CD11c-CD206+. **(B)** Relative abundance of B cells, T cells, neutrophils and dendritic cells (DCs) are plotted as percentage of CD45.2 positive events. Three different time points are represented. First row of panels: Before injections. Second row of panels: 16-days group. Third row of panels: 30-days group. There is no statistically significant difference in splenic cellular composition in unpaired two-tailed Student's t-test between the equivalent experimental group of *Pycard*$^{+/+}$and *Pycard*$^{-/-}$ mice at each individual time point. Error bar represents standard error of the mean (SEM). Each dot represents an individual mouse. **(C)** F4/80+ macrophages, M1-like MΦs and M2-like MΦs are plotted as percentage of CD45.2 positive events at three different time points. First lane panel represents baseline values whereas data of animals euthanized after 16 and 30 days are plotted in the second and third lane panels, respectively. ⁻ . Results are represented as mean ± standard error. Each dot represents one individual mouse.

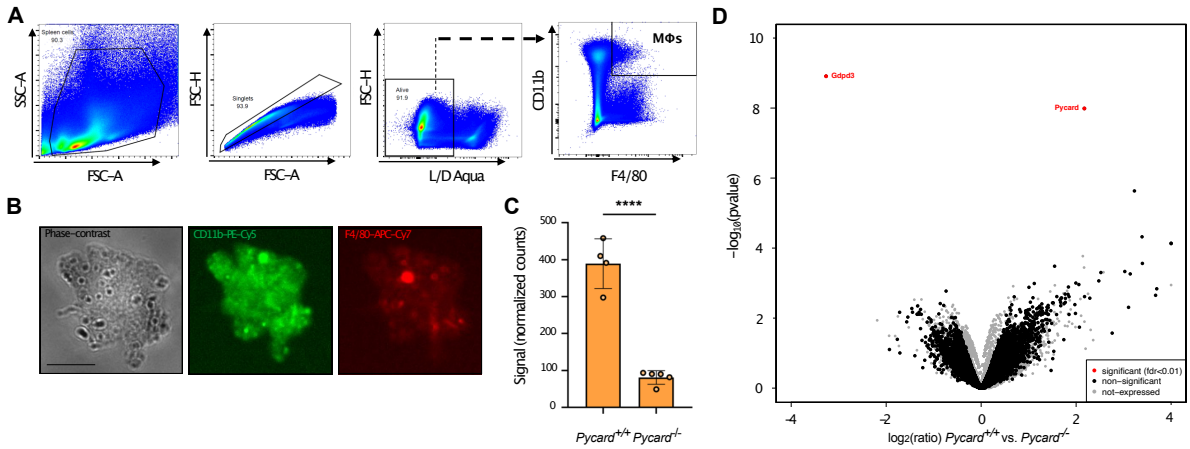

827

828 **Fig. S5**. **Transcriptional analysis of splenic macrophages from AA⁺ mice reveals mainly changes in *Pycard* expression**. **(A)**
829 Representative gating strategy of splenic macrophages flow cytometrically sorted from AA⁺ mice. Splenic cells were first gated
830 in an FSC-A vs. SSC-A plot followed by doublet and dead cell exclusion. Finally, CD11b+F4/80+ macrophages were bulk sorted
831 for transcriptomic analysis. **(B)** Representative images of splenic macrophages assessed **by** phase contrast and fluorescence
832 microscopy. . The middle and right panel confirms the presence of the two antibody-conjugated fluorophores PE-Cy5 and
833 APC-Cy7 that were used to identify CD11b+ and F4/80+ macrophages, respectively. Scale bar: approximately 10 µm. **(C)**
834 Scatter plot depicting normalized counts of ASC transcript reads. An unpaired, two-tailed Students' t-tests was performed.
835 Each dot represents one individual mouse. **(D) '**Volcano plot' of statistical significance vs. foldchange between *Pycard*$^{+/+}$and
836 *Pycard*$^{-/-}$ splenic macrophages from AA⁺ mice displays the most significantly and differentially expressed genes (in red). *
837 *P*<0.05, **** *P*<0.0001, ns: not significant.

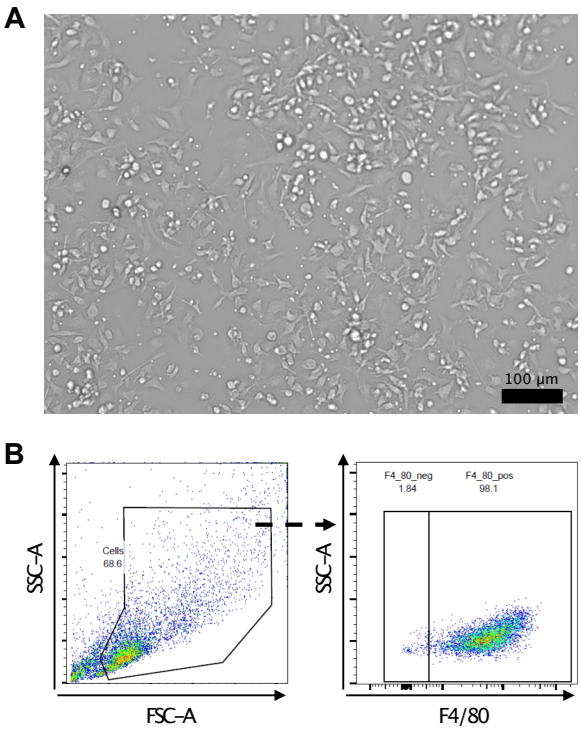

838

839 **Fig. S6**. ***In vitro*** **phagocytosis of SAA-stimulated BMDMs**. **(A)** Phase contrast micrograph of adherent and differentiated
840 BMDMs. **(B) Representative** flow cytometry gating for BMDM differentiation performed with anti-mouse F4/80 antibody, a
841 specific macrophage marker. Alive (not shown) F4/80+ cells represent differentiated BMDMs.

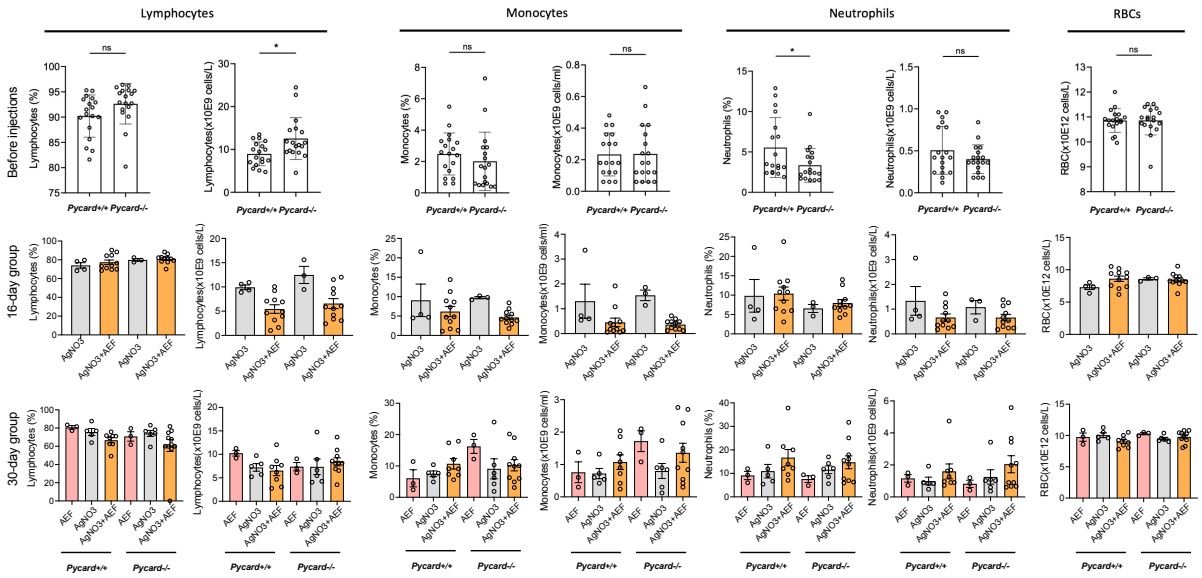

Fig. S7. **Complete blood count (CBC) assessment did not reveal significant changes in cellular blood compartments between AA-diseased and $AgNO_3$-only control animals**. Bar plots depicting the abundance of lymphocytes, monocytes, neutrophils red blood cells (RBCs) plotted in relative (%) as well as absolute values (cell numbers). Top panel represents before injections values of *Pycard*$^{+/+}$and *Pycard*$^{-/-}$ mice. Data of mice euthanized at day 16 and 30 are plotted in the middle and bottom panels, respectively. Results are represented as mean± standard deviation and SEM (error bars). Statistical analysis performed by unpaired two-tailed Student's t-test in CBC between the equivalent experimental group. Each dot represents one individual mouse. * P<0.05, ns: not significant.

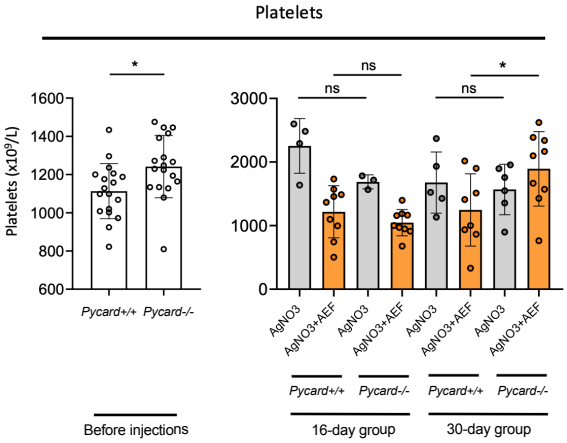

Fig. S8. **Altered platelet count in the absence of *Pycard* before injections and in AA disease state**. Bar plots depicting platelet counts from experimental mice and different time points are represented. Results are represented as mean± standard deviation (error bars). Platelet counts < 150 x10^9/L were excluded from analysis. Analysis was performed using unpaired two-tailed Student's t-tests. Each dot represents one individual mouse. * P<0.05, ns: not significant.

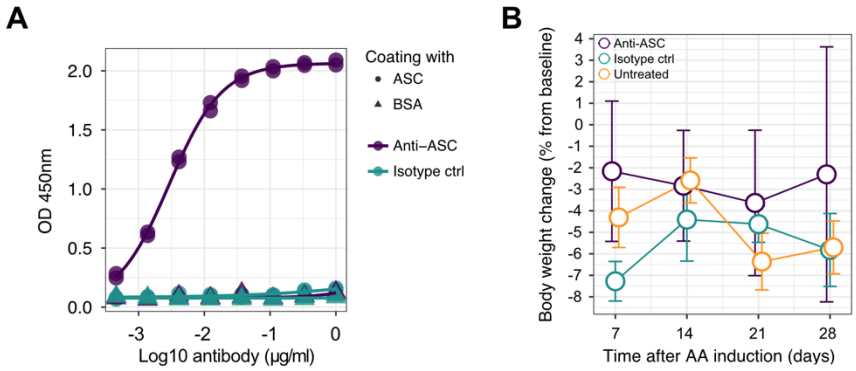

855

856 **Fig. S9**. **Anti-ASC antibody binding curve and body weight changes during immunotherapy. (A)** ASC-specific binding assay
857 for custom ASC and isotope control antibody. **(B)** Body weight change during the experiment (± SEM). Groups of 3 animals
858 were treated with anti-ASC antibodies, isotype control, or were left untreated. Statistics: Kruskal-Wallis test.

859

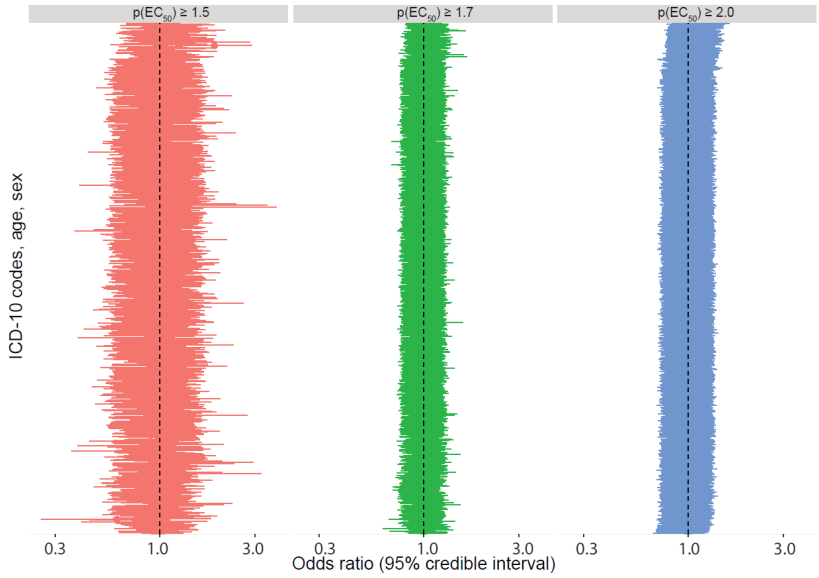

860

861 **Fig. S10**. **Sensitivity analysis of different p(EC_{50}) cutoff values using multiple logisitc regression analysis**. Different p(EC_{50})
862 cutoff values that range from 1.5 (left), 1.7 (middle) to 2.0 (right). Y-axis: ICD-10 codes, age, and sex, which have been
863 subjected to multiple logistic regression analysis using a Bayesian LASSO prior. X-axis: Odds ratio (OR) with 95% credible
864 interval.

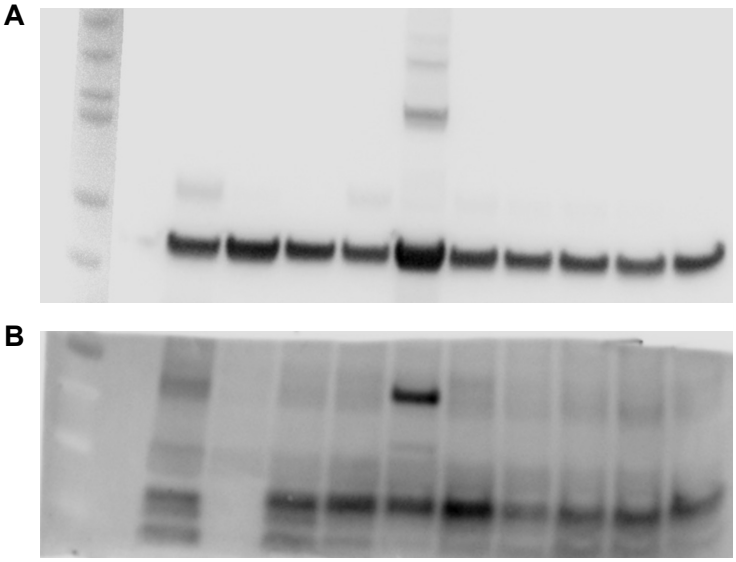

865

866 **Fig. S11**. **Uncropped and unmodified western blot images of Fig. 3**. **(A)** Uncropped image of western blot that was performed
867 on spleen homogenate of AA^+ mice and probed with anti-actin primary antibody. **(B)** Uncropped image of western blot that
868 was performed on spleen homogenate of AA^+ mice and probed with anti-SAA primary antibody for SAA detection. Of
869 important note, the upper main band visible in lane 5 most likely represents an oligomeric SAA species.

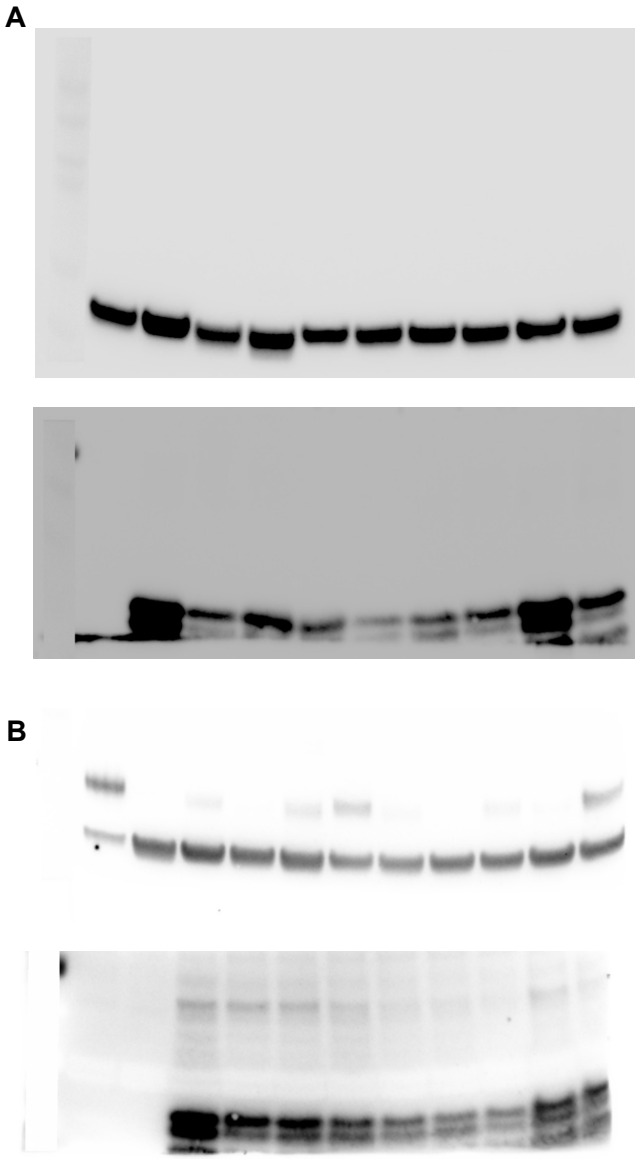

870

871 **Fig. S12**. **Uncropped Western blot images of Fig. 4**. **(A)** Uncropped image of Western blot that was performed on spleen
872 homogenate of AA^+ mice and probed with anti-actin primary antibody (upper blot). Uncropped image of Western blot that
873 was performed on spleen homogenate of AA^+ mice and probed with anti-SAA primary antibody for SAA detection (lower
874 blot). **(B)** Second representative Western blot. Uncropped image of Western blot that was performed on spleen homogenate
875 of AA^+ mice and probed with anti-actin primary antibody (upper blot). Uncropped image of Western blot that was performed
876 on spleen homogenate of AA^+ mice and probed with anti-SAA primary antibody for SAA detection (lower blot). Of note: Small
877 part of the membrane (last lane in the lower blot) was cut during processing.

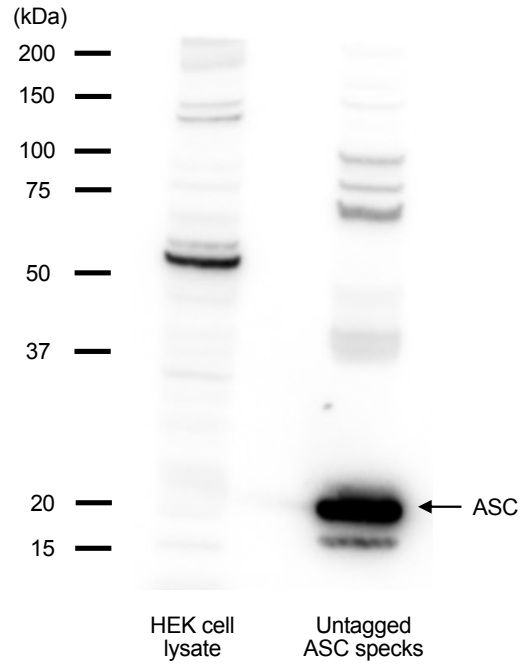

878

879 **Fig. S13. Purified ASC speck assessment by western blot**. Uncropped image of western blot that was performed on HEK cell
880 lysate (control, left lane) and purified untagged ASC specks (right lane) and probed with anti-ASC primary antibody for ASC
881 detection and assessment. Different bands and respective sized in the right lane represent ASC oligomers.

882 Supplemental tables

883 *Table S1. Accelerated SAA fibrillation in the presence of ASC specks.*

ASC specks (nr #) / Time ($t_{1/2}$)	0	1 x 10^5	2 x 10^5	5 x 10^5
Mean ± SD (hours)	98.83 ± 8.16	82.12 ± 8.73	79.22 ± 7.18	66.30 ± 4.10

884

885 *Table S2. Temporal SAA serum concentrations upon silver nitrate injection or AA induction.*

	Pycard$^{+/+}$		*Pycard*$^{-/-}$	
Group / Time (hrs)	$AgNO_3$ Mean ± SD (µg/ml)	$AgNO_3$+AEF Mean ± SD (µg/ml)	$AgNO_3$ Mean ± SD (µg/ml)	$AgNO_3$+AEF Mean ± SD (µg/ml)
Baseline	6.08 ± 6.44	1.49 ± 1.22	1.39 ± 0.99	1.27 ± 1.06
9h	84.44 ± 15.22	63.41 ± 36.12	49.08 ± 38.48	80.98 ± 49.2
24h	217.1 ± 124.5	125.4 ± 25.04	188.5 ± 120	231.9 ± 97.13
48h	118 ± 60.21	95.2 ± 40.01	106.5 ± 65.24	149 ± 34.62
72h	19.22 ± 10.65	16 ± 5.94	16.16 ± 7.7	26.69 ± 10.79
96h	3.28 ± 0.47	3.48 ± 1.55	4.38 ± 0.79	7.04 ± 5.77

886

887 *Table S3. HS-310-stained AA amyloid.*

	Pycard$^{+/+}$		*Pycard*$^{-/-}$	
Treatment / Group	$AgNO_3$ Mean ± SD (HS-310 area, %)	$AgNO_3$+AEF Mean ± SD (HS-310 area, %)	$AgNO_3$ Mean ± SD (HS-310 area, %)	$AgNO_3$+AEF Mean ± SD (HS-310 area, %)
16- day	-	6.13 ± 4.48	-	3.11 ± 2.46
30-day	-	17.63 ± 8.38	-	8.93 ± 6.5

888 *Table S4. Phagocytosis of Pycard$^{+/+}$ and Pycard$^{-/-}$ BMDMs.*

Genotype / Condition BMDMs	*Pycard*$^{+/+}$ Mean ± SD OD at 405 nm	*Pycard*$^{-/-}$ Mean ± SD OD at 405 nm	*p*-value	Sign.
Unstimulated	1.58 ± 0.03	1.53 ± 0.09	0.393	ns
Unstimulated + Cytochalasin D	0.32 ± 0.03	0.35 ± 0.03	0.077	ns
mSAA stimulated	1.72 ± 0.05	1.55 ± 0.11	0.002	sign.
mSAA stimulated + Cytochalasin D	0.34 ± 0.05	0.34 ± 0.01	0.630	ns

889

890 *Table S5. Genotype and sex of experimental animals.*

Group / Gender	AEF+$AgNO_3$ 16- and 30-day group	$AgNO_3$ only 16- and 30-day group	PBS only	AEF only	Total (n =)
Pycard$^{-/-}$ females (n =)	10	4	3	1	18
Pycard$^{-/-}$ males (n =)	14	6	0	3	23
Pycard$^{+/+}$ females (n =)	10	4	0	0	14
Pycard$^{+/+}$ males (n =)	12	6	3	3	24
Total (n =)	46	20	6	7	79

891

892 *Table S6. Genotype and age of experimental animals.*

Genotype / Treatment	*Pycard*$^{+/+}$	*Pycard*$^{-/-}$	*p*-value	Sign.
PBS-only (mean days ± SD)	77.67 ± 1.16	58.33 ± 19.63	0.164	ns
AEF-only (mean days ± SD)	80.33 ± 1.16	59.75 ± 15.17	0.071	ns
$AgNO_3$-only (mean days ± SD)	100.0 ± 20.07	94.8 ± 21.14	0.580	ns
$AgNO_3$ + AEF (mean days ± SD)	81.68 ± 12.11	88.96 ± 16.53	0.101	ns

Total (mean days ± SD)	86.08 ± 15.93	85.20 ± 21.18	0.837	ns

893

894 Table S7. Sex of experimental immunotherapy animals

Treatment / Gender	AEF+$AgNO_3$ (AA induction)	AA + anti-ASC abs	AA + isotype abs	Total (n =)
Pycard$^{+/+}$ females (n =)	4	3	4	11
Pycard$^{+/+}$ males (n =)	1	2	1	4
Total (n =)	5	5	5	15

895

896 *Table S8. Age of experimental immunotherapy animals.*

Genotype / Treatment	*Pycard*$^{+/+}$	*p*-value	Sign.
1.) AA induction only (mean weeks ± SD)	19.8 ± 5.59	1 vs 2: 0.959	ns
2.) AA + anti-ASC abs (mean weeks ± SD)	18.8 ± 4.76	2 vs 3: 0.974	ns
3.) AA + isotype abs (mean weeks ± SD)	19.6 ± 6.73	3 vs 1: 0.998	ns
Total (mean weeks ± SD)	19.4 ± 5.34	0.959	ns

897

898 Table S9. Western blot antibodies.

Antibody	Clone	Host / Conjugate	Source	Dilution (µl)
SAA recombinant rabbit monoclonal	D9H4L41	Rabbit	Invitrogen, #700830	1:200
Goat anti-rabbit IgG (H+L)	-	Goat/ HRP	Jackson Immuno, #111-035-045	1:5000
Anti-Actin antibody monoclonal	C4	Mouse	Merck, #MAB1501R	1:8000

Goat anti-mouse IgG (H+L)	-	Goat/ HRP	Jackson Immuno, #115-035-003	1:8000

899

900 Table S10. Flow cytometry antibodies.

Surface antigen	Fluorophore	Source	Dilution (µl)
Anti-mouse B220	Brilliant Violet 785	Biolegend, #103245	1:400
Anti-mouse CD11b	Brilliant Violet 650	Biolegend, #101239	1:400
Anti-mouse CD45.2	Pacific Blue	Biolegend, #109820	1:100
Anti-mouse CD3	Per/CPCy5.5	Biolegend, #100218	1:100
Anti-mouse Gr-1	PE/Cy5	eBioscience™, #15-5931-82	1:400
Anti-mouse CD206	PE	Biolegend, #141705	1:100
Anti-mouse F4/80	APC-eFluor 780	eBioscience™, #47-4801-82	1:200
Anti-mouse MHCII	Alexa Fluor® 700	Biolegend, #107621	1:800
Anti-mouse CD11c	APC	eBioscience™, #17-0114-82	1:400

901

902 Table S11. Antigens used for the high-throughput antibody profiling.

Antigen	Application	Coating concentration	Source	Product #
ASC-C-his	ELISA	1 µg/ml	Matthias Geyer, ISB, University of Bonn [15]	
human recPrP$_{23-230}$	ELISA	1 µg/ml	In-house [50]	
Tau441	ELISA	2 µg/ml	In-house	
SARS-CoV-2 Spike ECD	ELISA	1 µg/ml	[75]	
nAra h 2	ELISA	1 µg/ml	Indoor Biotechnologies	NA-AH2-1
ASC-PYD	ELISA	1 µg/ml	Mabylon AG, Schlieren	

ASC-CARD	ELISA	1 µg/ml	Mabylon AG, Schlieren	
LAG3	ELISA	1 µg/ml	AcroBiosystems	LA3-H5222
TIM3	ELISA	1 µg/ml	AcroBiosystems	TM3-H5229

903

904 Table S12. Antibodies used for the high-throughput antibody profiling.

Species	Target	Dilution/Concentration range	Brand name	Product #
(HRP) Goat	anti-human IgG	1:4000	Jackson	109-035-098
(HRP) Goat	anti-mouse IgG	1:2000	Jackson	115-035-003
(HRP) Goat	anti-rabbit IgG	1:2000	Jackson	111-035-045
Mouse	anti-ASC	1 µg/ml - 0.06 ng/ml	Santa Cruz	sc-514414
Human	anti-human PrP	1 µg/ml - 0.06 ng/ml	In-house	
Mouse	anti-Tau441	1 µg/ml - 0.06 ng/ml	Sigma-Aldrich	05-804
Mouse	anti-his	1 µg/ml - 1,38 ng/ml	Invitrogen	37-2900
Rabbit	anti-ASC	1 µg/ml - 1,38 ng/ml	Mabylon AG, Schlieren	MY6745

905

References

1. Papa R, Lachmann HJ. Secondary, AA, Amyloidosis. Rheum Dis Clin North Am 2018;44:585-603.
2. Brunger AF, Nienhuis HLA, Bijzet J, et al. Causes of AA amyloidosis: a systematic review. Amyloid 2020;27:1-12.
3. Lee JY, Hall JA, Kroehling L, et al. Serum Amyloid A Proteins Induce Pathogenic Th17 Cells and Promote Inflammatory Disease. Cell 2020;180:79-91 e16.
4. Sack GH. Serum amyloid A - a review. Mol Med 2018;24:46.
5. Ye RD, Sun L. Emerging functions of serum amyloid A in inflammation. J Leukoc Biol 2015;98:923-9.
6. Westermark GT, Westermark P. Serum amyloid A and protein AA: molecular mechanisms of a transmissible amyloidosis. FEBS Lett 2009;583:2685-90.
7. Dubrey SW, Cha K, Simms RW, et al. Electrocardiography and Doppler echocardiography in secondary (AA) amyloidosis. Am J Cardiol 1996;77:313-5.
8. Chamling B, Drakos S, Bietenbeck M, et al. Diagnosis of Cardiac Involvement in Amyloid A Amyloidosis by Cardiovascular Magnetic Resonance Imaging. Front Cardiovasc Med 2021;8:757642.
9. Heneka MT, Kummer MP, Latz E. Innate immune activation in neurodegenerative disease. Nat Rev Immunol 2014;14:463-77.
10. Heneka MT, Golenbock DT, Latz E. Innate immunity in Alzheimer's disease. Nat Immunol 2015;16:229-36.
11. Anders HJ, Muruve DA. The inflammasomes in kidney disease. J Am Soc Nephrol 2011;22:1007-18.
12. Aguzzi A. The protean roles of neuroinflammation in trauma, infections, autoimmunity and neurodegeneration. Semin Immunol 2022;61-64:101655.
13. Jang S, Jang WY, Choi M, et al. Serum amyloid A1 is involved in amyloid plaque aggregation and memory decline in amyloid beta abundant condition. Transgenic Res 2019;28:499-508.
14. Ising C, Venegas C, Zhang S, et al. NLRP3 inflammasome activation drives tau pathology. Nature 2019;575:669-673.
15. Venegas C, Kumar S, Franklin BS, et al. Microglia-derived ASC specks cross-seed amyloid-β in Alzheimer's disease. Nature 2017;552:355-361.
16. Dansokho C, Heneka MT. Neuroinflammatory responses in Alzheimer's disease. J Neural Transm (Vienna) 2018;125:771-779.
17. Fernandes-Alnemri T, Alnemri ES. Assembly, purification, and assay of the activity of the ASC pyroptosome. Methods Enzymol 2008;442:251-70.
18. Eisenberg D, Jucker M. The amyloid state of proteins in human diseases. Cell 2012;148:1188-203.
19. Balci-Peynircioglu B, Waite AL, Schaner P, et al. Expression of ASC in renal tissues of familial mediterranean fever patients with amyloidosis: postulating a role for ASC in AA type amyloid deposition. Exp Biol Med (Maywood) 2008;233:1324-33.
20. Scarpioni R, Ricardi M, Albertazzi V. Secondary amyloidosis in autoinflammatory diseases and the role of inflammation in renal damage. World J Nephrol 2016;5:66-75.
21. Pastore S, Paloni G, Gattorno M, et al. PReS-FINAL-2240: Serum amyloid protein a concentration in CAPS patients treated with anti IL1B. Pediatric Rheumatology 2013;11:P230.
22. Niemi K, Teirilä L, Lappalainen J, et al. Serum amyloid A activates the NLRP3 inflammasome via P2X7 receptor and a cathepsin B-sensitive pathway. J Immunol 2011;186:6119-28.
23. Chen W, Qiang X, Wang Y, et al. Identification of tetranectin-targeting monoclonal antibodies to treat potentially lethal sepsis. Sci Transl Med 2020;12.
24. Gaiser AK, Bauer S, Ruez S, et al. Serum Amyloid A1 Induces Classically Activated Macrophages: A Role for Enhanced Fibril Formation. Front Immunol 2021;12:691155.
25. Lundmark K, Vahdat Shariatpanahi A, Westermark GT. Depletion of spleen macrophages delays AA amyloid development: a study performed in the rapid mouse model of AA amyloidosis. PLoS One 2013;8:e79104.
26. Sponarova J, Nuvolone M, Whicher C, et al. Efficient amyloid A clearance in the absence of immunoglobulins and complement factors. Am J Pathol 2013;182:1297-307.
27. Kisilevsky R, Boudreau L. Kinetics of amyloid deposition. I. The effects of amyloid-enhancing factor and splenectomy. Lab Invest 1983;48:53-9.
28. Magy N, Liepnieks JJ, Benson MD, et al. Amyloid-enhancing factor mediates amyloid formation on fibroblasts via a nidus/template mechanism. Arthritis Rheum 2003;48:1430-7.

29. Kennel SJ, Macy S, Wooliver C, et al. Phagocyte depletion inhibits AA amyloid accumulation in AEF-induced huIL-6 transgenic mice. Amyloid 2014;21:45-53.
30. Nyström SN, Westermark GT. AA-Amyloid is cleared by endogenous immunological mechanisms. Amyloid 2012;19:138-45.
31. Pepelnjak M, de Souza N, Picotti P. Detecting Protein-Small Molecule Interactions Using Limited Proteolysis-Mass Spectrometry (LiP-MS). Trends Biochem Sci 2020;45:919-920.
32. Schopper S, Kahraman A, Leuenberger P, et al. Measuring protein structural changes on a proteome-wide scale using limited proteolysis-coupled mass spectrometry. Nat Protoc 2017;12:2391-2410.
33. Schurch PM, Malinovska L, Hleihil M, et al. Calreticulin mutations affect its chaperone function and perturb the glycoproteome. Cell Rep 2022;41:111689.
34. Cappelletti V, Hauser T, Piazza I, et al. Dynamic 3D proteomes reveal protein functional alterations at high resolution in situ. Cell 2021;184:545-559 e22.
35. Feng Y, De Franceschi G, Kahraman A, et al. Global analysis of protein structural changes in complex proteomes. Nat Biotechnol 2014;32:1036-44.
36. Piazza I, Kochanowski K, Cappelletti V, et al. A Map of Protein-Metabolite Interactions Reveals Principles of Chemical Communication. Cell 2018;172:358-372 e23.
37. Holfeld A, Schuster D, Sesterhenn F, et al. Systematic identification of structure-specific protein–protein interactions. bioRxiv 2023:2023.02.01.522707.
38. Fernandes-Alnemri T, Wu J, Yu JW, et al. The pyroptosome: a supramolecular assembly of ASC dimers mediating inflammatory cell death via caspase-1 activation. Cell Death Differ 2007;14:1590-604.
39. Srinivasula SM, Poyet JL, Razmara M, et al. The PYRIN-CARD protein ASC is an activating adaptor for caspase-1. J Biol Chem 2002;277:21119-22.
40. Eisenbarth SC, Colegio OR, O'Connor W, et al. Crucial role for the Nalp3 inflammasome in the immunostimulatory properties of aluminium adjuvants. Nature 2008;453:1122-6.
41. Gabay C, Kushner I. Acute-phase proteins and other systemic responses to inflammation. N Engl J Med 1999;340:448-54.
42. Simons JP, Al-Shawi R, Ellmerich S, et al. Pathogenetic mechanisms of amyloid A amyloidosis. Proc Natl Acad Sci U S A 2013;110:16115-20.
43. Erdem E, Erdem D, Dilek M, et al. Red cell distribution width and mean platelet volume in amyloidosis. Clin Appl Thromb Hemost 2014;20:334-7.
44. Bakan A, Oral A, Alışır Ecder S, et al. Assessment of Mean Platelet Volume in Patients with AA Amyloidosis and AA Amyloidosis Secondary to Familial Mediterranean Fever: A Retrospective Chart - Review Study. Med Sci Monit 2019;25:3854-3859.
45. Rolfes V, Ribeiro LS, Hawwari I, et al. Platelets Fuel the Inflammasome Activation of Innate Immune Cells. Cell Rep 2020;31:107615.
46. Sponarova J, Nyström SN, Westermark GT. AA-amyloidosis can be transferred by peripheral blood monocytes. PLoS One 2008;3:e3308.
47. Couturier J, Stancu IC, Schakman O, et al. Activation of phagocytic activity in astrocytes by reduced expression of the inflammasome component ASC and its implication in a mouse model of Alzheimer disease. J Neuroinflammation 2016;13:20.
48. Pandey A, Shen C, Feng S, et al. Cell biology of inflammasome activation. Trends Cell Biol 2021;31:924-939.
49. Schenk D. Amyloid-beta immunotherapy for Alzheimer's disease: the end of the beginning. Nat Rev Neurosci 2002;3:824-8.
50. Senatore A, Frontzek K, Emmenegger M, et al. Protective anti-prion antibodies in human immunoglobulin repertoires. EMBO Mol Med 2020;12:e12739.
51. Sevigny J, Chiao P, Bussiere T, et al. The antibody aducanumab reduces Abeta plaques in Alzheimer's disease. Nature 2016;537:50-6.
52. Sonati T, Reimann RR, Falsig J, et al. The toxicity of antiprion antibodies is mediated by the flexible tail of the prion protein. Nature 2013;501:102-6.
53. Emmenegger M, De Cecco E, Lamparter D, et al. Continuous population-level monitoring of SARS-CoV-2 seroprevalence in a large European metropolitan region. iScience 2023;26:105928.
54. Lamparter D, Jacquat RPB, Riou J, et al. Code repository for SARS-CoV-2 seroprevalence study. 1.0.0 ed, 2022.
55. Mariathasan S, Newton K, Monack DM, et al. Differential activation of the inflammasome by caspase-1 adaptors ASC and Ipaf. Nature 2004;430:213-8.
56. de Alba E. Structure, interactions and self-assembly of ASC-dependent inflammasomes. Arch Biochem Biophys 2019;670:15-31.

57. Vajjhala PR, Mirams RE, Hill JM. Multiple binding sites on the pyrin domain of ASC protein allow self-association and interaction with NLRP3 protein. J Biol Chem 2012;287:41732-43.
58. Oroz J, Barrera-Vilarmau S, Alfonso C, et al. ASC Pyrin Domain Self-associates and Binds NLRP3 Protein Using Equivalent Binding Interfaces. J Biol Chem 2016;291:19487-501.
59. Vahdat Shariat Panahi A, Hultman P, Öllinger K, et al. Lipid membranes accelerate amyloid formation in the mouse model of AA amyloidosis. Amyloid 2019;26:34-44.
60. Richards DB, Cookson LM, Barton SV, et al. Repeat doses of antibody to serum amyloid P component clear amyloid deposits in patients with systemic amyloidosis. Sci Transl Med 2018;10.
61. Claus S, Meinhardt K, Aumuller T, et al. Cellular mechanism of fibril formation from serum amyloid A1 protein. EMBO Rep 2017;18:1352-1366.
62. Rocken C, Kisilevsky R. Comparison of the binding and endocytosis of high-density lipoprotein from healthy (HDL) and inflamed (HDL(SAA)) donors by murine macrophages of four different mouse strains. Virchows Arch 1998;432:547-55.
63. Moretti J, Blander JM. Increasing complexity of NLRP3 inflammasome regulation. J Leukoc Biol 2021;109:561-571.
64. Bodin K, Ellmerich S, Kahan MC, et al. Antibodies to human serum amyloid P component eliminate visceral amyloid deposits. Nature 2010;468:93-7.
65. Lundmark K, Westermark GT, Nystrom S, et al. Transmissibility of systemic amyloidosis by a prion-like mechanism. Proc Natl Acad Sci U S A 2002;99:6979-84.
66. Nilsson KP, Ikenberg K, Aslund A, et al. Structural typing of systemic amyloidoses by luminescent-conjugated polymer spectroscopy. Am J Pathol 2010;176:563-74.
67. Sjolander D, Rocken C, Westermark P, et al. Establishing the fluorescent amyloid ligand h-FTAA for studying human tissues with systemic and localized amyloid. Amyloid 2016;23:98-108.
68. Wahlström N, Edlund U, Pavia H, et al. Cellulose from the green macroalgae Ulva lactuca: isolation, characterization, optotracing, and production of cellulose nanofibrils.
69. Martín-Sánchez F, Gómez AI, Pelegrín P. Isolation of Particles of Recombinant ASC and NLRP3. Bio Protoc 2015;5.
70. Meisl G, Kirkegaard JB, Arosio P, et al. Molecular mechanisms of protein aggregation from global fitting of kinetic models. Nat Protoc 2016;11:252-72.
71. Yanagita T, Murata Y, Tanaka D, et al. Anti-SIRP. JCI Insight 2017;2:e89140.
72. Ono Y, Nagai M, Yoshino O, et al. CD11c+ M1-like macrophages (MΦs) but not CD206+ M2-like MΦ are involved in folliculogenesis in mice ovary. Sci Rep 2018;8:8171.
73. Arlt A, von Bonin F, Rehberg T, et al. High CD206 levels in Hodgkin lymphoma-educated macrophages are linked to matrix-remodeling and lymphoma dissemination. Mol Oncol 2020;14:571-589.
74. Nawaz A, Aminuddin A, Kado T, et al. CD206. Nat Commun 2017;8:286.
75. Emmenegger M, Kumar SS, Emmenegger V, et al. Anti-prothrombin autoantibodies enriched after infection with SARS-CoV-2 and influenced by strength of antibody response against SARS-CoV-2 proteins. PLoS Pathog 2021;17:e1010118.
76. Emmenegger M, Fiedler S, Brugger SD, et al. Both COVID-19 infection and vaccination induce high-affinity cross-clade responses to SARS-CoV-2 variants. iScience 2022;25:104766.
77. Emmenegger M, De Cecco E, Hruska-Plochan M, et al. LAG3 is not expressed in human and murine neurons and does not modulate alpha-synucleinopathies. EMBO Mol Med 2021;13:e14745.
78. Jagusiak A, Rybarska J, Konieczny L, et al. Amyloids, Congo red and the apple-green effect. Acta Biochim Pol 2019;66:39-46.